Island growth and step instabilities on flat and vicinal surfaces

Marko Rusanen

Laboratory of Physics
Helsinki University of Technology

Fysiikan laboratorio
Teknillinen korkeakoulu

DISSERTATION 120 (2003)

ISLAND GROWTH AND STEP INSTABILITIES ON FLAT AND VICINAL SURFACES

Marko Rusanen

Laboratory of Physics
Helsinki University of Technology
Espoo, Finland

Dissertation for the degree of Doctor of Science in Technology to be presented with due permission of the Department of Engineering Physics and Mathematics, Helsinki University of Technology for public examination and debate in Auditorium E at Helsinki University of Technology (Espoo, Finland) on the 26th of February, 2003, at 12 o'clock noon.

Dissertations of Laboratory of Physics, Helsinki University of Technology
ISSN 1455-1802

Dissertation 120 (2003):
Marko Rusanen: Island growth and step instabilities on flat and vicinal surfaces
ISBN 951-22-6373-4 (print)
ISBN 951-22-6374-2 (electronic)

OTAMEDIA OY
ESPOO 2003

Abstract

Surface physics aims at understanding the basic atomistic processes and mechanisms responsible for the variety of observed structures during surface growth. In addition, surface growth has important consequences in modern technological applications. Molecular beam epitaxy (MBE) is an established method to grow surface structures, admitting also modeling surface growth through simple microscopic processes such as diffusion and deposition of atoms. The rather limited parameter range in MBE where smooth layer-by-layer growth is realized can be extended, e.g., with ion assisted deposition techniques. Thus new microscopic processes are added to traditional MBE growth. Customarily island growth and step-flow are treated as separate growth modes. Consequently, there does not exist a growth model which includes all relevant aspects of surface growth in a realistic way.

The aim of this thesis is to bridge the gap between these traditional approaches. Including other microscopic processes in addition to deposition and surface diffusion introduces new scaling relations and length scales. In addition, not only the scaling of the growth structures but also their stability is of importance. Moreover, unstable growth often possesses a dynamically selected length scale. It is of interest to understand the behavior of these new time and length scales and their scaling properties when constructing more realistic growth models.

To this end, we consider various aspects of surface growth. First, we simulate island growth with aggregation, fragmentation, and deposition on flat surfaces. The generalized rate equations are introduced, and the scaling forms for the island size distributions and the mean island size are proposed and compared with simulation results. Next, stability of circular islands is studied by generalizing the rectangular case to radial geometry. A stability criterion for the island radius is derived in the long wavelength limit. Then, stability of step edges on vicinal surfaces is considered. The simulation results demonstrate the dynamical wavelength selection with a quantitative prediction for the selected wavelength as well as the mechanism behind the instability. The average shape of the unstable step patterns is found to have an invariant form, insensitive to the parameters of the model. Finally, the simulations extended to include both island growth and step edge instability reveal that these growth modes are coupled with a new length scale, and are inpendent only in the submonolayer regime.

Preface

In high school academic studies seemed to be some distant and vague thing that I surely did not intend to do. In the beginning of my physics studies at University of Helsinki a PhD thesis seemed to be some distant and vague thing, not for me please. And when starting the graduate studies at Helsinki University of Technology I thought that teaching is something I'll never do. And now, as the thesis is finished, perhaps it is wise not to mention any new things I'll never do.

The most of the work for this thesis was done in Laboratory of Physics at Helsinki University of Technology, during 1998–2002. I would like to thank my excellent instructors Dr. Ismo Koponen and Prof. Tapio Ala-Nissilä for guidance. Ismo has such an attitude towards research and life in general that I very much appreciate. Tapio has shown the good practices of research and trusted that I can do my work. I also want to acknowledge the pre-examiners of my thesis, Prof. Miroslav Kotrla and Prof. Kai Nordlund for the careful reading of the manuscript.

Thanks also to all my coauthors and the members of the Statistical Physics and Materials Science group. Especially I want to thank Dr. Jarkko Heinonen and my roommate Dr. Joonas Asikainen. Jarkko gave me invaluable help in the beginning of my research. Discussions with Joonas have been enjoyable and useful as well as his help in many practical issues.

I would like also to thank administrative personnel of Laboratory of Physics, financial support from Academy of Finland, Project 50508, and travel support from Magnus Ehrnrooth Foundation and Väisälä Foundation.

Finally, the warmest thanks belong to my wife Ritva, who has given me her unconditional love and support during all these years.

Espoo, February 2003

Marko Rusanen

Contents

List of Publications

This thesis consists of an overview and the following publications:

I. I. Koponen, M. Rusanen, and J. Heinonen, "Island size distributions in submonolayer growth with mobile islands and breakup", Physical Review E **58**, 4037–4040 (1998).

II. M. Rusanen, I.T. Koponen, and T. Ala-Nissila, "Meandering instability of curved step edges on growth of a crystalline cone", Surface Science **507-510**, 305–309 (2002).

III. M. Rusanen, I.T. Koponen, J. Heinonen, and T. Ala-Nissila, "Instability and wavelength selection during step flow growth of metal surfaces vicinal to fcc(001)", Physical Review Letters **86**, 5317–5320 (2001)

IV. M. Rusanen, I.T. Koponen, T. Ala-Nissila, C. Ghosh, and T.S. Rahman, "Morphology of ledge patterns during step flow growth of metal surfaces vicinal to fcc(001)", Physical Review B **65**, 041404:1–4 (2002).

V. M. Rusanen, I.T. Koponen, and J. Kallunki, "Mixing length scales: step meandering and island nucleation on vicinal surfaces", submitted to Surface Science (7 pages) (2002).

The author has had an active part in all stages of research. He has been involved in planning and conducting the research. He has written and developed the simulation programs. He has performed most of the simulations reported in Publication I, all simulations and numerical work in Publications II, III, and V, all analytical calculations in Publication IV, and data analysis in all Publications. He has written Publications II and V, the first draft of Publication IV, and contributed actively on writing other Publications. In addition, the thesis contains unpublished results from Ref. [1] on the improved particle coalescence method developed by the author.

1

Introduction

During the past few decades crystal surfaces have attracted considerable interest, mainly due to advent of atomic resolution imaging techniques [2]. Novel experiments reveal many previously unknown features and phenomena on surfaces which need to be explained. In particular, self-assembling patterns and growth instabilities form challenging topics in surface physics needing communication between experiments and theoretical models. The models can be tested and improved by comparing model predictions with experimental results. On the other hand, the predictions from theoretical models could guide new experimental efforts. Also technological applications require proper understanding of the means to obtain surfaces with known properties. For example, it would not be possible to manufacture modern computer chips without a detailed knowledge of surface growth on semiconductor materials. Consequently, growth of surface structures provides intriguing examples of both equilibrium and nonequilibrium physics [3].

Molecular beam epitaxy (MBE) is a method to grow thin films on surfaces with good quality [4]. Its essential advantage is the ability to control the growth process in the atomistic scale (below 10^{-7} meters). MBE also enables theoretical modeling based on a relatively simple picture of relevant physical processes during growth which are schematically depicted in Fig. 1.1. The growth scenario is as follows. Atoms are randomly deposited from the supersaturated gas phase onto a surface where they are adsorbed. These adsorbed atoms (adatoms) perform random walk on a surface due to thermal coupling with the lattice vibrations. As more adatoms appear on a surface they eventually nucleate clusters of adatoms (islands) or attach to pre-existing pinning sites such as other islands, step edges, or dislocations. Adatom desorption back to the gas phase can be ignored since typically growth during MBE occurs at rather low temperatures. Thus the mor-

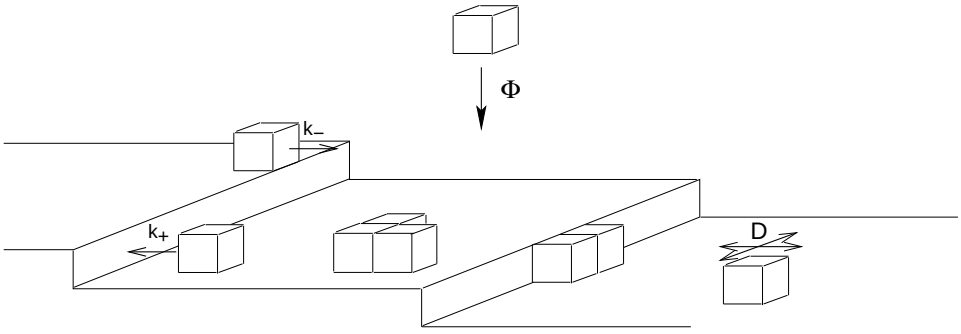

Figure 1.1. A schematic picture of a vicinal (stepped) surface during MBE growth. Atoms are deposited at the rate Φ onto a surface where they are adsorbed. Adatoms diffuse on flat parts of the surface with a diffusion coefficient D, and attach to the step edges with rates k_- (from above) and k_+ (from below). If Φ is large enough island nucleation on terraces takes place.

phology and dynamics of growing layers are completely determined by the interplay between deposition of atoms and relaxation of the surface profiles through surface diffusion [5].

In surface growth it is usually desirable to grow layers in a smooth layer-by-layer mode. On flat surfaces atomic layers are formed by nucleation and growth of adatom islands. If the deposition flux is small relative to surface diffusion these islands are two-dimensional and the first layer completes before the second one appreciably nucleates [6,7]. Layer-by-layer growth is also achieved on vicinal surfaces which are miscut relative to a high-symmetry crystal plane. Such surfaces consist of steps and high-symmetry terraces between them. For small enough fluxes deposited atoms preferentially attach to step edges instead of nucleating new islands. Thus the step edges uniformly advance as more material is deposited onto a surface resulting in smooth step-flow growth. Surfaces are often, however, subject to instabilities under growth conditions. It is important to know the mechanisms producing unstable growth since usually instabilities lead to non-uniform layers. By understanding the processes responsible for instabilities, one can suppress them during surface growth.

With MBE the parameter range where smooth layer-by-layer growth is obtained is rather limited. Large fluxes or low temperatures lead to formation of three-dimensional structures. One can, however, utilize other growth techniques such as ion-beam assisted deposition [8] or sputtering deposi-

tion [9] in order to obtain smooth growth. These techniques can be also modeled including new microscopic processes to the MBE scenario. For example, during ion-beam assisted deposition island mobility and dissociation processes are induced [10]. In these cases new processes lead to new scaling laws and length scales. Moreover, since the processes are reversible there is no guarantee that island growth and step-flow can be treated as separate processes as conventionally assumed. It is possible that island growth and step-flow are equally important and lead to completely new features of growth in addition to novel scaling relations and length scales.

The aim of this thesis is to take a step towards a general picture of surface growth where both island growth and step-flow are taken into account in a realistic way. This is a formidable task, however, and to this end the work is focused on some of the important aspects of pattern formation during surface growth. These are the emergence of new scaling relations due to additional growth processes, study of stability of island boundaries and surface steps and corresponding length scales, and a general growth situation where both island growth and step-flow are present.

Island growth forms an important part of all surface growth problems since it acts as a basis for further structure formation [11, 12]. In homoepitaxial systems where the deposited material is the same as the substrate the basic processes such as aggregation [13], deposition [14], and detachment [15], and length scales and scaling laws [16,17] related to island growth are rather well understood. These scaling ideas and corresponding rate equations in island growth are reviewed in Chapter 2.

Stability of surface steps is important in step-flow growth on vicinal surfaces since step instability leads eventually to break-down of the step-flow mode and formation of three-dimensional structures [18]. Unstable step morphologies result due to asymmetric mass currents across [19] or along [20] the step edges. The associated length scale in the former case is well understood. Chapter 3 discusses instabilities related to step-flow growth, namely Bales-Zangwill instability [19] and the kink Ehrlich-Schwoebel effect [20].

The simulation methods are reviewed in Chapter 4. The Bortz-Kalos-Lebowitz algorithm enables us to simulate surface growth on vicinal surfaces in a semi-realistic way with realistic system sizes, energy parameters, and temperature and flux ranges. The particle coalescence method used in island growth simulations, and in particular, a new improved version of it, are introduced.

The central results of the thesis are reported in Chapter 5. These are essentially aimed at fulfilling the gaps between the existing traditional approaches in island growth and step-flow. The results would help to construct a more general growth model, e.g., in a continuum level.

First, the scaling laws and length scales in island growth with aggregation, fragmentation, and deposition are discussed. The rate equations describing the growth process are presented and the scaling forms for the size distributions and the mean island size are proposed. The validity of the scaling functions are confirmed by simulations. New results for the scaling exponents (see Appendix A) and an equation for the mean island size are derived supplementing Publication I.

The meandering instability in radial geometry is then discussed. Not only is structure formation such as island growth important but also the stability of growth structures. Here the focus is on the stability of circular islands in the initial stages of growth. The purpose is to examine whether the stability of island shapes has any effects on growth in the time and length scales of interest. The correction terms to the rectangular case due to curvature and the smallest unstable island size are derived.

Following this, we consider the case where the meandering instability and consequent wavelength selection are controlled by kink Ehrlich-Schwoebel barriers along the step edges. A quantitative prediction for the wavelength is shown to agree with the simulations as well as experiments. The average meander profile is shown to have an invariant shape which is rather insensitive to the external parameters such as temperature or flux.

Finally, the combined growth simulations with island nucleation and step meandering instability are discussed. In realistic growth conditions both island growth and step-flow are present. It is of interest to know to what extent these growth modes can be regarded as separate processes. The simulation results show that island formation and meandering instability are mutually independent only in the submonolayer regime but develop a nontrivial coupling when islands and steps begin to coalesce.

The thesis ends with Chapter 6 containing a summary and discussion followed by two appendices where the scaling exponents and the scaling function for the mean island size are derived, and the details of the meandering instability in radial geometry are given.

2

Island growth on flat surfaces

Island growth on a flat surface during submonolayer deposition plays an important part in surface growth since it forms the basis for all further growth [11, 12]. Information about the microscopic processes responsible for the surface structures can be obtained through the scaling properties of, e.g., the mean island size, the scaling function of the island size distribution [16], or the island separation [21]. In the following, concepts and different processes related to island growth are introduced.

2.1 Nucleation of islands

Growth of surface structures e.g. with MBE involves deposition of atoms onto a surface, subsequent diffusion of those adatoms on the surface, and eventually nucleation of adatom clusters, commonly called islands. As atoms are deposited onto a surface they are adsorbed and begin to randomly migrate at non-zero temperatures. If there are only a negligible number of other possible attachment sites, adatoms eventually meet each other and form together an island. The smallest island size which is more likely to grow than to decay is defined as the critical island size [17]. For example, at sufficiently low temperatures an adatom pair (dimer) can be taken as the critical size.

Nucleation of islands proceeds as long as adatoms form new islands instead of attaching to the existing ones. A stationary state is reached when the number of islands N remains constant and only island sizes change. Rate equation studies predict that N scales as a power-law with respect to the surface diffusion coefficient D and the incoming flux Φ [22,23]. This implies that one can measure the surface diffusion coefficient D by calculating the

number of islands on a surface [21]. The scaling relation is given by [22]

$$N \sim \left(\frac{D}{\Phi}\right)^{-\chi}, \tag{2.1}$$

where χ is the scaling exponent which depends on the spatial dimension d, microscopic surface processes, and the critical island size [17, 22–24]. For a given model χ is well-defined usually in some temperature or flux range. This so-called mean-field (MF) form is valid and useful in the parameter region where χ is a constant. For example, it does not apply in compound semiconductor systems [25], or if long-range adatom interactions are important [26].

One can also argue that N scales with a single length scale ℓ_n [23], called the nucleation length, leading to the relation $\ell_n \sim (D/\Phi)^{\chi/d}$, where d is spatial dimension. This enables one to calculate the scaling exponent χ within the minimal model of stable and immobile dimers [23]. Following arguments in Refs. [23, 27] one obtains the expression for the nucleation length:

$$\ell_n \sim \left(\frac{D}{\Phi}\right)^{1/(2d+2)}, \tag{2.2}$$

where numerical factors of order unity have been omitted, and the scaling exponent $\chi = d/(2d+2)$ is obtained. If temperature is high enough to break a dimer the scaling exponent is modified [24]. Also on vicinal surfaces the nucleation length is more difficult to calculate since the number of incoming adatoms onto the surface region is not necessarily given by $\Phi\ell^d$ [28].

2.2 Scaling of the size distributions and the mean size

A powerful method to study film growth in the submonolayer regime is based on scaling ideas. This lies on the assumption that quantities of interest can be scaled at arbitrary time (in a scaling regime) with some characteristic length scale. For example, in the scaling regime the island size distributions are completely determined by the knowledge of the mean island size [17]. During island growth the mean size naturally sets an intrinsic length scale for the system. From the size distribution one can deduce the uniformity of growing islands and possibly manipulate the distributions by tuning the

external parameters. Scaling also implies that one can predict the properties of the system with different parameter values and at different times by measuring them at one point in the parameter space or at one moment of time. Then the quantities of interest with another set of parameter values can be obtained simply by scaling them using the appropriate scaling relations.

During submonolayer island growth the mean island size is defined by [16,17]

$$\bar{s} = \frac{\sum_s s^2 n_s}{\sum_s s n_s}, \tag{2.3}$$

where the island size distribution $n_s(t)$ is the areal density of islands of size s in the system. In the following, $n_s(t) \equiv \langle n_s(\mathbf{r}, t) \rangle$, i.e. the size distributions are understood to be averaged over an ensemble of systems or a sufficiently large surface region [17].

Scaling forms for the mean island size can be proposed by examining how $\bar{s}$ qualitatively behaves as a function of time or other parameters. These scaling forms can be justified and the corresponding scaling exponents determined from rate equations, as described in the following Sections. For irreversible growth $\bar{s}$ grows monotonically in time or coverage and it is plausible to expect that [16]:

$$\bar{s} \sim \theta^{\beta}, \tag{2.4}$$

where $\theta = \Phi t$ is the coverage, t is the deposition time, and β is the dynamic scaling exponent. Another scaling relation can be obtained with respect to the external parameters. If the external flux is small, adatoms landing onto the surface have enough time to diffuse and attach to islands before deposition of the next atom. For large fluxes there are many adatoms diffusing around and nucleating new islands leading to a smaller mean island size. The opposite is true at low temperatures where adatoms diffuse slowly compared to high temperature regime. Consequently, one finds a scaling relation with respect to the diffusion coefficient of an adatom D and the external flux Φ [16, 17]:

$$\bar{s} \sim \mathcal{R}^{\chi}, \tag{2.5}$$

where $\mathcal{R} = D/\Phi$ and χ is the scaling exponent whose value depends on d and the microscopics of the system, e.g. surface diffusion processes [23, 24].

At the onset of growth the only relevant length scale in the system is the mean island size. In this submonolayer regime a scaling ansatz for the size

distribution function is proposed [16, 17, 29]:

$$n_s \sim \frac{\theta}{\bar{s}^\tau} f(s/\bar{s}), \tag{2.6}$$

where τ is the scaling exponent to be specified later, and $f(x)$ is a scaling function independent of θ and $\mathcal{R}$. The scaling function is normalized as $\int f(x)\mathrm{d}x = 1$. It must be emphasized that this scaling form is rather general, applying equally well e.g. to scaling of the cluster size distribution function in percolation problems [30]. The specific functional form of the scaling function depends on the details of the model [16, 31], e.g. on d, whether diffusion is isotropic, and whether detachment of adatoms from islands is operative. The point is that, within the model, the scaled size distributions collapse into one universal curve independent of θ and $\mathcal{R}$. Note that the scaling form Eq. (2.6) does not require $\bar{s}$ to follow a power law behavior [17].

2.3 Rate equations

Insight into island growth or clustering process in general can be obtained from rate equations. These are a coupled set of deterministic differential equations describing the time evolution of n_s. Despite that introduced already a century ago by Smoluchowski [32] rate equations are still used in various applications ranging from materials science [22], biology [33], and financial analysis [34] to astrophysics [35]. In fact, in many cases rate equations provide a simple method to get reliable information of the complicated problem. In the following, aggregation, irreversible island growth, aggregation with fragmentation, and reversible growth are reviewed.

2.3.1 Aggregation

The set of the rate equations for clustering follows when one counts all aggregation events increasing or decreasing the number of clusters of size s. This is experimentally realized, e.g., in aerosol systems or on surfaces where islands have a non-zero diffusion coefficient. One ends up with the Smoluchowski rate equation [32, 36]:

$$\frac{\mathrm{d}n_s}{\mathrm{d}t} = \frac{1}{2}\sum_{i+j=s} K(i,j) n_i n_j - \sum_{i=1}^{\infty} K(s,i) n_s n_i, \tag{2.7}$$

where $K(i,j)$ is the aggregation kernel (also called the coagulation or reaction kernel), denoting the probability per unit time to aggregate two clusters with sizes i and j. The first term on the right hand side denotes the gain by aggregation of smaller islands whereas the second term is the loss term due to aggregation events between an island of size s and any other size i. This equation can be derived from the master equation [37] using the method of compounding moments [38]. It must be emphasized that since n_s is an average over a surface region or an ensemble, spatial correlations are not taken into account in the rate equations. Thus the rate equations describe the system in the mean-field (MF) limit.

In many cases of interest the kernels $K(i,j)$ can be reasonably approximated to have simple homogeneous forms [13,39]. These homogeneous forms admit the scaling solutions of Eq. (2.7). The homogeneity of the kernel $K(i,j)$ implies [13]:

$$K(ai, aj) = a^{\lambda} K(i,j), \tag{2.8}$$

where $a > 0$ is a constant and λ is called the homogeneity exponent. Physically relevant values are $\lambda < 2$ since the reactivity of an island cannot grow faster than its size [13]. In the cases interest to us $\lambda < 1$, corresponding to non-gelling solutions [13]. Conservation of the total mass of the system $M = \sum_k k n_k$ in aggregation yields $\tau = 2$ in the scaling form Eq. (2.6). From the Smoluchowski equation it follows that the mean size obeys asymptotically ($t \to \infty$) a simple power law [13, 29]:

$$\bar{s} \sim t^z, \tag{2.9}$$

where the dynamic scaling exponent is

$$z = \frac{1}{1-\lambda}, \tag{2.10}$$

and depends only on the homogeneity exponent of the kernel.

The scaling function $f(x)$ introduced in the scaling ansatz for the size distribution [Eq. (2.6) with $\tau = 2$] can be calculated in principle for a given model (i.e. for a given aggregation kernel). Unfortunately this is analytically possible only in some restricted cases. For example, in the case of interest to us the kernel has the form $K(i,j) \sim i^{-\mu} + j^{-\mu}$ ($\mu > 0$) in which case the scaling function turns out to be [13]

$$f(x) \sim x^{-1} \exp[-x^{-\mu} M_0 / (\mu M_{-\mu})], \tag{2.11}$$

where the moments are defined as $M_k = \sum_s s^k n_s$.

2.3.2 Irreversible growth

The rate equations introduced in the previous Section can be also applied to study irreversible island growth during submonolayer deposition. In the case of immobile islands and irreversible growth (size of an island can only increase) only aggregation events between an island and an adatom are taken into account. One obtains the rate equations for the size distributions [17]:

$$\frac{\mathrm{d}n_s}{\mathrm{d}t} = Dn_1\sigma_{s-1}n_{s-1} - Dn_1\sigma_s n_s, \tag{2.12}$$

where the first term takes into account for the increase of the number of islands of size s due to adatom attachment into the island of size $s-1$, and the second term losses due to similar process for the island of size s. For monomers one obtains [17]:

$$\frac{\mathrm{d}n_1}{\mathrm{d}t} = \Phi - 2D\sigma_1 n_1^2 - Dn_1 \sum_{i=2}^{\infty} \sigma_s n_s, \tag{2.13}$$

where the first term is due to deposition of adatoms onto a surface, and σ_s is the capture number for an island of size s. All terms due to direct capture from the incoming flux are omitted. The capture rates contain microscopic information of the small scale processes and long-range correlations between islands [17]. In the point island approximation it is sufficient to set $\sigma = const.$ [16] but when island geometry has to be taken into account it holds generally that $\sigma = \sigma(s)$ [17]. Also, non-local adsorbate mediated interactions can be taken into account in a reasonable way in σ_s [40].

In the case where island geometry has to be taken into account the capture numbers play an important role determining the correct size distributions. One could solve the capture numbers self-consistently assuming that the surrounding of an island is independent of its size in the case of immobile islands which correctly reproduces the adatom and total island densities [17]. The full size distributions were resolved only recently when strong correlations between island sizes and separations were realized [41, 42]. This leads to a contribution to σ_s from the correlations in island sizes and separations [41]. The correlations between the capture zones and island separations can be constructed in terms of tesselation based on the Voronoi area for each island [43]. Such treatment produces correctly the average quantities as well as the size distributions both in the point-island approximation and the compact island case [43]. However, as far as generic features of growth are

concerned the correlations between island sizes and separations can be omitted. In addition, it turns out that correlations are negligible when island mobility or fragmentation are taken into account.

2.3.3 Aggregation and fragmentation

To take into account reversible island processes in addition to aggregation, i.e. adatom detachment (e.g. at high temperatures) or fragmentation of islands (e.g. during ion bombardment of a surface), one modifies the rate equations for aggregation to include terms of the form $F(i,j)n_{i+j}$ to break an island of size $s = i + j$ into two smaller islands with sizes i and j. If the fragmentation kernel has a homogeneous form, one expects to obtain scaling solutions also in this case. One customarily chooses the fragmentation kernel to be of the form $F(i,j) = F_0(i+j)^\alpha$ for binary fragmentation [44,45]. The probability to choose an island of size s is n_s, and let us assume that any of those $s-1$ bonds can be broken with equal probability. Thus, the total probability to break a bond in an island of size s is $n_s(s-1)^{-1}p(s)$ where $p(s)$ is the probability for breaking a bond. It is commonly assumed that $p(s)$ has the form $p(s) \propto (s-1)s^\alpha$ which leads to the above form for $F(i,j)$. With these assumptions the rate equations read [44–46]:

$$\frac{\mathrm{d}n_s}{\mathrm{d}t} = \frac{1}{2}\sum_{i+j=s}\left[K(i,j)n_i n_j - F(i,j)n_{i+j}\right] - \sum_{i=1}^{\infty}\left[K(i,s)n_i n_s - F(i,s)n_{i+s}\right]. \tag{2.14}$$

The scaling forms for the mean island size are different from the pure aggregation case. Since aggregation decreases the number of islands and increases the mean island size and fragmentation does the opposite, one could assume that after some characteristic time the system reaches a stationary state [44,47]. Define the ratio $\kappa = F_0/K_0$ which measures the relative importance between fragmentation and aggregation. Before the steady state is reached the system is in the aggregation-dominated regime which implies that $\bar{s}$ scales as in Eq. (2.9). In the steady state the mean size is constant in time but the characteristic time scales as $\tau \sim \kappa^{-a}$. One assumes that also $\bar{s}$ scales as [47]

$$\bar{s} \sim \kappa^{-y}, \tag{2.15}$$

where the scaling exponent y has the value [44,45]

$$y = \frac{1}{-\lambda + \alpha + 2}. \tag{2.16}$$

This depends only on the homogeneities of aggregation λ and fragmentation α. These scaling forms suggest that one can make a scaling ansatz for the mean size [47] $\bar{s} = \tau^z \Psi(T)$, where $T = t/\tau$ and $\Psi(T)$ is a scaling function independent of κ for $T \ll 1$, and independent of time for $T \gg 1$.

The size distribution function is shown to scale as in Eq. (2.6). In the case of interest to us the functional form for the scaling function $f(x)$ turns out to be [44]

$$f(x) \sim x^{\delta+1} \mathrm{e}^{-cx}, \tag{2.17}$$

where $\delta = 1 - \lambda + \alpha$ [48] and c is a constant[†].

2.3.4 Reversible growth

As previously discussed including reversible processes such as fragmentation leads to new scaling relations and length and time scales. For example, in aggregation with fragmentation a new time scale for approach to a stationary state can be defined with a new scaling exponent. In island growth in many practical cases reversible processes take place, for example at high temperatures adatom detachment from islands. Adatom detachment can be taken into account in the rate equations (2.12) by including the corresponding terms of the form n_s/τ_s [49], where τ_s is the mean rate for adatoms to escape from an island of size s. Detachment can be included in a self-consistent way in capture numbers for islands in analog to irreversible growth [49]. Detachment during growth leads to a different time dependence, e.g., for the mean island size which grows logarithmically instead of a power law [50, 51]. Generalized reversible processes in island growth with aggregation, fragmentation, and deposition are discussed in Chapter 5.

[†]Note that in Ref. [47] expressions $\delta = 1-\lambda+\alpha$ (for $\lambda > 1+\alpha; \lambda > 1+2\alpha$), $\delta = 1-(1+\lambda)/2$ (for $\lambda > 1; \lambda < 1+2\alpha$), and $\delta = 1-\lambda$ (for $\lambda < 1+\alpha; \lambda < 1$) are obtained.

3

Instabilities of surface steps

Generally in surface growth islands grow on terraces between steps. Moreover, growing islands are also stepped structures. Both island boundaries and steps on vicinal surfaces are one-dimensional objects, and consequently even in equilibrium they are rough at any finite temperature. During surface growth unstable step edge structures can be produced, e.g., due to asymmetric mass currents along the different surface directions. While the instability of the straight step edges due to the Ehrlich-Schwoebel barrier is well known, relatively less studied case is the curved steps. Here the established models of the instability at straight steps are reviewed which also form a basis for a discussion about more complicated structures. The meandering of curved steps is discussed in Chapter 5.

3.1 Bales-Zangwill instability

Energy barriers related to microscopic processes can have significant consequences on surface morphologies during growth. For example, on many surfaces an adatom close to the downhill step edge is more likely to be reflected back than crossing the edge due to the Ehrlich-Schwoebel (ES) barrier [52, 53]. The extra barrier can be understood on the basis of low coordination of an adatom at the intermediate position between the initial and final states during step crossing. The large ES barrier induces different effects on growth morphology: It is responsible for instabilities associated with mound formation on flat surfaces [54] and meandering of surface steps on vicinal surfaces [19], but also stabilization of vicinal surfaces against step bunching [55].

For a non-vanishing ES barrier adatoms nucleate new islands on top of existing ones leading to growth of mounds on flat surfaces. Moreover, for

an infinite ES barrier steep mounds appear quickly and growing smooth layers is hindered [56]. On vicinal surfaces the ES barrier stabilizes any step spacing other than the average distance L thus preventing step bunching. If a terrace is larger than L it receives more mass from the deposition flux than the smaller terraces and consequently the step edge in the uphill direction advances faster than the other steps. On the other hand, if a terrace is smaller than L the step in the uphill direction has a smaller velocity than other steps until the average terrace width is reached. However, the same ES barrier produces a meandering instability of steps. If there is a fluctuation at the step edge adatoms on a terrace attach to the protrusion more likely than to other parts of the edge. For a non-zero ES barrier this effect is asymmetric with respect to the lower and the upper terraces. Thus protrusions will gather more mass from the lower than from the upper terrace as atoms are deposited onto a surface. This leads to meandering of steps and is the origin of the Bales-Zangwill (BZ) instability [19] discussed in the following. Moreover, simulations using a solid-on-solid (SOS) model have shown that after the BZ instability has developed a secondary instability sets in leading to mounds also on a vicinal surface [18].

Quantitatively the meandering of step edges can be studied on the basis of the Burton-Cabrera-Frank (BCF) model of crystal growth [57] and the Mullins-Sekerka instability [58]. BZ showed [19] that small fluctuations in the linear order produce morphologically unstable step edges. In the spirit of BCF the adatom concentration ρ obeys the diffusion equation on a terrace [57]:

$$\frac{\partial \rho}{\partial t} = D\nabla^2\rho - \frac{\rho}{\tau} + \Phi, \tag{3.1}$$

where D is the adatom diffusion coefficient, τ is a characteristic time for desorption, and Φ is the incoming adatom flux. One can define a length scale $x_s = \sqrt{D\tau}$ which corresponds to the scale an adatom diffuses before desorption back to the gas phase. Defining a new variable $u = \rho - \tau\Phi$ Eq. (3.1) becomes the Helmholtz equation for u in the stationary limit [19]:

$$\nabla^2 u - \frac{u}{x_s^2} = 0, \tag{3.2}$$

where the stationary condition $\partial_t \rho \approx 0$ can be justified if the steps move slowly compared with the rate at which the adatom concentration relaxes to its equilibrium value [19]. For large step velocities a convective term must be included [59].

The problem is fully specified when the boundary conditions are given. The normal velocity of the step is [59]

$$v_n = \Omega D \left(\nabla\rho \,|_+ - \nabla\rho|_- \right) \cdot \mathbf{n}, \tag{3.3}$$

where Ω is the atomic area, $\nabla\rho|_\pm$ are the contributions to the velocity from the lower and upper terrace, respectively, and $\mathbf{n}$ is the unit vector locally perpendicular to the edge. The local velocities are [59]

$$\pm D\nabla\rho \cdot \mathbf{n} = k_\pm \left[\rho - \rho_{\rm eq}\right]|_\pm, \tag{3.4}$$

where $k_\pm$ are the kinetic coefficients describing atom attachment to the step from the lower and upper terraces, and $\rho_{\rm eq}$ is the equilibrium adatom concentration at the step edge. For a curved edge one uses the Gibbs-Thomson relation [60]:

$$\rho_{\rm eq} = \rho^0_{\rm eq} \exp(\Omega\gamma\kappa/k_BT) \approx \rho^0_{\rm eq} + \Gamma\kappa, \tag{3.5}$$

where $\rho^0_{\rm eq}$ is the equilibrium concentration at the straight step, κ is the local curvature of the edge, $\Gamma = \Omega\rho^0_{\rm eq}\gamma/(k_BT)$, γ is the step stiffness, and k_BT is thermal energy.

The solution of Eq. (3.1) for the straight step is $u_0(x) = a_0 \sinh(x/x_s) + b_0 \cosh(x/x_s)$, where x is the coordinate along the step direction. The coefficients a_0 and b_0 are determined by the boundary conditions. The linear stability analysis is now performed around the straight step solution. One introduces a periodic perturbation of the straight step at y with a particular wave number q as $\xi(x) = y + \epsilon \exp(\mathrm{i}qx + \omega t)$, where ϵ is a small parameter and $\omega(q)$ is the growth rate. If $\omega > 0$ the straight step is unstable. The solution to the first order in ϵ is $u(x,y) = u_0(x) + \epsilon[A_q \sinh(\Lambda_q y) + B_q \cosh(\Lambda_q y)] \exp(\mathrm{i}qx + \omega t)$, where $\Lambda_q = \sqrt{q^2 + x_s^{-2}}$. In the linear analysis this is put into the step velocity and solved in the first order in ϵ. On the other hand, the velocity is also given by $v_n = v_0 + \omega(q)\epsilon \exp(\mathrm{i}qx + \omega t)$, where v_0 is the velocity of the straight step. From these one finds the expression [19]:

$$\omega(q) = (d_- - d_+)g(q) - q^2 f(q), \tag{3.6}$$

where the functions $g(q)$ and $f(q)$ are positive for all q (see Ref. [19] for the complete expressions), and $d_\pm = D/k_\pm$.

From Eq. (3.6) we conclude that the step edge is always stable if $d_- \leq d_+$, i.e. $k_- \geq k_+$. For $k_- < k_+$ there is a band of wave numbers and

wavelengths $\lambda = q/2\pi$ which correspond to $\omega > 0$ for certain parameter combinations. One would then observe unstable step patterns with the wavelength corresponding to the maximum of ω, i.e. perturbations with the wavelengths $\lambda > \lambda_c$ will grow, and the fastest growing mode corresponds to $\lambda_u = \sqrt{2}\lambda_c$. In the limit where desorption vanishes ($\tau \to \infty$) one obtains:

$$\lambda_u \propto \left(\frac{D}{\Phi}\right)^{1/2}, \tag{3.7}$$

where the proportionality constant equals to $4\pi\sqrt{\Omega\gamma c_{\mathrm{eq}}^0/(k_B T L^2)}$. This expression prevails also in the non-linear regime [61].

For further reference we also give here the expressions for the critical wave number defined through $\omega(q_c) = 0$ in the limiting cases. We have for $L \gg x_s$ [19]:

$$x_s q_c = \begin{cases} \sqrt{\frac{x_s}{\xi}}, & x_s q_c \gg 1; \\ \sqrt{\frac{4}{3}(1-2\xi)}, & x_s q_c \ll 1, \end{cases} \tag{3.8a}$$

where $\xi = \Gamma/(\tau\Delta\Phi)$ is the capillary length and $\tau\Delta\Phi = \tau\Phi - \rho_{\mathrm{eq}}^0$. For $L \ll x_s$ (and $L^2 q_c^2 \ll 1$) we obtain [19]:

$$x_s q_c = \sqrt{\frac{L}{2\xi}}. \tag{3.8b}$$

From these expressions it is clear that there is a competition between the stabilizing and destabilizing effects, viz. diffusion x_s and line tension ξ, respectively. For example, as $x_s \to \infty$ step flow is unstable for a finite value of ξ at long wavelengths. The generalization to the radial geometry is given in Chapter 5.

3.2 Kink Ehrlich-Schwoebel effect

The meandering instability observed in SOS simulations [18] and also the first experimental results were interpreted through the BZ explanation [62]. Recent STM experiments on vicinal Cu surfaces demonstrated that the selected wavelength does not quantitatively agree with the BZ prediction [63].

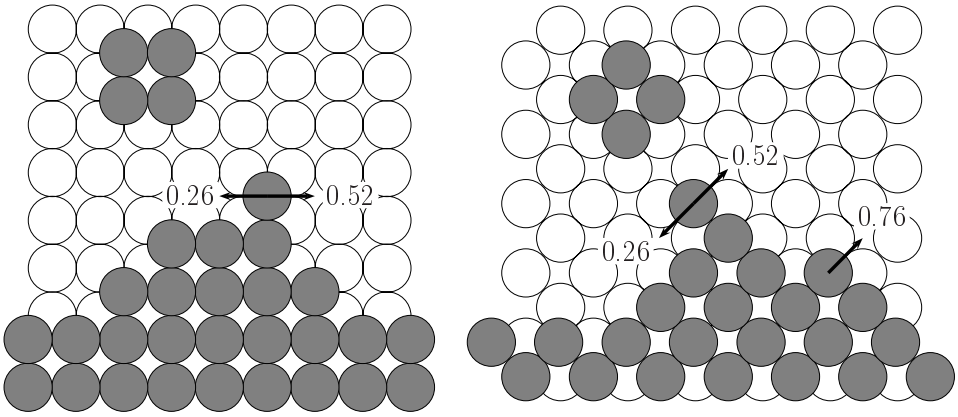

a) Close-packed step **b)** Open step

Figure 3.1. A top view of a fcc surface with a) close-packed and b) open step edges. Solid circles correspond to the upper and open circles the lower terrace. Energy barriers on a Cu surface [67] for a few processes denoted by the arrows are given in the units of eV.

The first simulations with the simplified SOS model suggested that the kink Ehrlich-Schwoebel effect (KESE) may lead to formation of a step instability [64, 65]. In addition, SOS simulations have shown that both the BZ and KESE instabilities are possible, depending on the relative importance of edge diffusion [66]. However, quantitative data of the selected wavelength and the structure of the patterns were still unresolved. Also, most results were for the weak KESE while one assumes that on Cu surfaces the opposite is true. Calculations of energy barriers indicate the extra barrier about 0.25 eV for kink rounding at close-packed step edges [67] but experimental evidences of KES barrier are still few (see, however, Refs. [68, 69]). In any case, if it does exist, the KES barrier could have rather large consequences on interpretation of experiments, especially determining the value of the ES barrier via the time-dependent step correlation function [70].

During the growth of a vicinal surface incoming adatoms landing on terraces will eventually attach to step edges if terrace nucleation is suppressed. On many surfaces an adatom at the edge preferentially diffuses along the step rather than detaches back to the terrace (for simple metal surfaces, see Ref. [67]). This leads to the formation of one-dimensional (1D) islands at the edge. As the first row of 1D islands at the edge have grown large enough subsequent adatoms coming to the step attach on top of them. Now, KESE

for a non-zero kink ES barrier ensures that almost all adatoms stay on top of the first-row islands and cross the kink sites only rarely. Thus KESE induces destabilizing mass currents along the up-kink direction and unstable structures onto the step edges, in analog of the mounding instability on flat surfaces [20].

The above discussion of the destabilizing character of KESE applies well to close-packed steps where the KES barrier is believed to exist. For example, on fcc surfaces one can have both close-packed and open steps (see Fig. 3.1) with different energy barriers at the edge. Based on symmetry arguments one can argue that KESE is actually stabilizing open steps [20, 71]. This is further elucidated in Fig. 3.1. At open steps adatoms diffuse along steps via a two-step process. Thus protrusions have triangular shapes with close-packed sides. An adatom attaching to the side of the triangle preferentially seeks the two-fold coordinated site close to the edge since at the tip of the triangle it experiences the KES barrier. Of course, it might be the case that for open steps strain effects could play an important part and influence diffusion processes at the edge.

3.2.1 Wavelength of patterns

Define a scale L_n as a characteristic length of an edge above which islands form, i.e. at the edges with $L > L_n$ nucleation occurs. In the case of dimer nucleation in 1D the length is given by [22, 72]

$$L_n \propto \left(\frac{D_s}{\Phi_s}\right)^{1/4},$$

where $D_s \propto \exp(-E_s/k_BT)$, E_s is the diffusion barrier along the straight edge, and $\Phi_s = \Phi L$ is the flux onto the edge. For weak KESE the wavelength λ of unstable step patterns can be determined from the linear stability analysis and turns out to be [72, 73]

$$\lambda \propto \sqrt{\frac{L_n^3}{L_s}}, \tag{3.9}$$

where $L_s = \exp[(E_k - E_s)/k_BT] - 1$ is the kink ES length [20] and E_k is the KES barrier. For strong KESE Eq. (3.9) is no longer valid. In this case one can assume that λ is set by dimer nucleation at the onset of growth so that $\lambda \approx L_n$.

3.2.2 Mass currents along the edge

Due to mass conservation at the step edge, the edge profile $\zeta(x,t)$ obeys the continuity equation [20, 72]:

$$\frac{\partial \zeta}{\partial t} = \Phi_s - \frac{\partial J_{\text{tot}}}{\partial x}, \tag{3.10}$$

where Φ_s is the incoming flux onto the edge, and J_{tot} is the total mass current along the edge. The total current decomposes into terms $J_{\text{tot}} = J_k + J_e + J_n + J_{\text{SB}}$. Define the variables $M(x) = \partial_x \zeta$ and $m(x) = M/\sqrt{1+M^2}$. Expressing the currents in terms of $M(x)$ and $m(x)$, and embedding some of the constants into x and t by appropriate scaling gives the stabilizing Gibbs-Thomson current including the edge diffusion [61, 74]:

$$\begin{aligned} J_e &= \frac{2D_S\tilde{\Gamma}}{\Phi}\left(\frac{1}{\sqrt{1+M^2}} + \frac{D_L}{D_S L}\right)\frac{1}{\sqrt{1+M^2}}\frac{\partial}{\partial x}\left(\frac{\partial_x M}{(1+M^2)^{3/2}}\right) \\ &= \frac{2D_S\tilde{\Gamma}}{\Phi}\left(\sqrt{1-m^2} + \frac{D_L}{D_S L}\right)\sqrt{1-m^2}(\partial_{xx} m), \end{aligned} \tag{3.11}$$

the current onto the step from the flux [61, 74]:

$$\begin{aligned} J_d &= L\frac{M}{1+M^2} \\ &= Lm\sqrt{1-m^2}, \end{aligned} \tag{3.12}$$

the current which breaks the front-back symmetry of the step profiles [72, 73]:

$$\begin{aligned} J_{\text{SB}} =& \frac{D_S\tilde{\Gamma}L}{\Phi}\frac{\partial_x M}{(1+M^2)^{3/2}}\frac{1}{1+M^2}\frac{\partial}{\partial x}\left(\frac{\partial_x M}{(1+M^2)^{3/2}}\right) \\ &+ \frac{L^2}{3}\frac{M}{1+M^2}\frac{\partial_x M}{(1+M^2)^{3/2}}\left(\sqrt{1+M^2} + \frac{2}{\sqrt{1+M^2}}\right) \\ =& -\frac{D_S\tilde{\Gamma}L}{\Phi}(\partial_x m)(\partial_{xx} m)\sqrt{1-m^2} + \frac{L^2}{3}m(\partial_x m)(3-m^2), \end{aligned} \tag{3.13}$$

and the destabilizing current due to KESE [20]:

$$\begin{aligned} J_k &= \frac{(1-|M|)M}{\sqrt{1+M^2}(|M| + L_n^{-1})^2} \\ &= \frac{m(\sqrt{1-m^2} - |m|)\sqrt{1-m^2}}{(|m| + \ell_c^{-1}\sqrt{1-m^2})^2}. \end{aligned} \tag{3.14}$$

In these expressions $D_S = Dc_{\mathrm{eq}}^0$ is the macroscopic diffusion coefficient on a terrace, $D_L \propto \exp(-E_L/k_BT)$ is the macroscopic diffusion coefficient along step edges, E_L is the corresponding hopping barrier, and $\tilde{\Gamma} = \tilde{\gamma}/k_BT$ is the scaled step stiffness. In all cases the lattice constant is equal to one.

These currents are phenomenological in nature, and contain qualitatively relevant behavior of the system. We have not included, e.g., the stabilizing currents arising from adatom detachment from the edge or random nucleation which both would have a contribution of the form $J = K\partial_{xxx}\zeta$, where K is depends on the slope of the profile [73]. However, for low temperatures adatom detachment is not a relevant process. Also, if one is interested in the stationary profile nucleation is a rare event for large slopes and can be neglected. Moreover, in the case of nucleation this form of the current applies only for weak KESE [73].

4

Methods

Conventional Metropolis Monte Carlo simulations (a hit-and-miss method) of surface growth become extremely slow at low temperatures since usually many microscopic processes with different energy and time scales are present. Improved methods, for example Monte Carlo with the Bortz-Kalos-Lebowitz algorithm [75], can be orders of magnitudes faster than Metropolis Monte Carlo at low temperatures. In the case of rate equations numerical integration is not always straightforward, especially when a large number of coupled differential equations is needed. The particle coalescence method (PCM) [76] is a method to simulate rate equations in a simple way. In the following the fast Monte Carlo technique and PCM are reviewed and a new improved version of PCM for simulating rate equations is introduced.

4.1 The Bortz-Kalos-Lebowitz Monte Carlo algorithm

In order to reach typical time scales and system sizes in atomistic growth simulations one must perform a coarse-graining procedure from the microscopic description of the system to a larger scale. For example, lattice vibrations (phonons) in metals have typically a characteristic time scale of 10^{-13} seconds [77] whereas in many surface growth problems characteristic times from 10^{-3} up to seconds are encountered. This clearly makes direct Molecular Dynamics type of simulations unfeasible and one is directed to use Monte Carlo (MC) techniques in addition to continuum models and rate equations.

The traditional MC method is based on the theory of Markov chains which assumes that the next state of the system depends only on the present

state [78]. In a MC simulation using the Metropolis importance sampling [78] one starts with the system in the initial configuration c. Then the final configuration c' is chosen with the uniform probability $1/N$, where N is the total number of possible transitions. The attempt to change the state is successful with probability $\nu_{c\to c'}/\nu_{\max}$, where $\nu_{c\to c'}$ is the rate for the transition from c to c', and $\nu_{\max}$ is the maximum of the all transition rates. Usually $\nu_{\max}$ is normalized to unity, and the transition probability is given by the Boltzmann factor $\exp(-\Delta E/k_BT)$, where $\Delta E = E_f - E_i$ is the energy difference between the final and initial states. If the attempt is accepted the system moves into the new configuration, otherwise it is left in the initial state. In this way the system always evolves toward equilibrium, i.e. (at least locally) to the minimum energy configuration [78]. The advantage of the traditional MC is that one needs to know explicitly only the relative transition probabilities. On the other hand, the drawback is unsuccessful events. For example, in the case of thermally activated transitions the Boltzmann factor involves the inverse temperature in the exponential. Thus the hit-and-miss method becomes extremely slow in computation time at low temperatures due to many unsuccessful attempts to change the configuration. As a consequence the actual evolution of the system is slow at low temperatures and one needs many MC steps between the measurements in order to collect uncorrelated data. The same applies in any MC simulation where the probability to accept the next state is small.

To increase the success ratio of the trial moves one can use the Bortz-Kalos-Lebowitz (BKL) algorithm [75]. The idea is to always choose an event with the correct probability, hence the success ratio is always unity. In this way the time step becomes stochastic since for every transition there is associated a waiting time the system stays in the initial configuration. In traditional MC this waiting time is (on the average) explicitly taken into account through unsuccessful attempts. In BKL every attempt is successful and so the time step must be drawn correctly. Since the events are evenly placed on a time axis the time step Δt is exponentially distributed with the decay constant equal to the total transition rate Γ_c of the configuration c:

$$P(\Delta t) = \Gamma_c \exp(-\Gamma_c \Delta t). \tag{4.1}$$

The inverse of the total transition rate is equal to the time the system stays in the initial state. Note that since time is now a stochastic variable one must be careful when measuring time-dependent observables. In fact, one should divide the time interval into bins and calculate the average time for

each bin. This introduces also errors in time measurements in addition to errors in observables.

The drawback of the BKL method is that at every step the correct value of Γ_c is needed. This implies that after every transition new transition rates at each site must be calculated (if they have changed). The task becomes feasible if the energy barriers associated with the transitions depend only locally of the neighborhood of a site. In this case the local configuration at each site can be determined and the corresponding transition rate associated with that particular neighborhood. Thus the whole algorithm highly relies on the discrete nature of the problem. However, there has been a recent attempt to extend the method also to a continuous set of transitions [79].

Another drawback of BKL is that it is much more complicated to implement on a computer than the Metropolis method. For example, to choose an event with the correct weight one must know the rates of all sites in the system. One can order all sites with the same rate into the same class, choose first between the classes, and then choose the site within the class with the uniform probability [75, 80]. After the transition the changed classes must be updated. Another way is to construct a binary tree where searching an event is fast [81] but the updating the tree is slightly more complicated than with the event classes.

4.2 Particle coalescence method

Calculating the average quantities in island growth from MC simulations can be done in reasonable computing time. However, to calculate e.g. the size distribution function roughly the same statistics is needed for every island size to have good data. This can be a very heavy computational task with a realistic MC simulation. Also, if one needs to study the island population dynamics using a realistic description of island morphology, complications due to geometric effects arise. To circumvent these problems one can use the particle coalescence method (PCM) [76] which is an example of a traditional MC method. The idea of PCM is to treat all islands as point-like, i.e. an island occupies only a single lattice site with a label carrying its size. In this way the rate kernels $K(i, j)$ can be specified exactly without any complications arising from island geometry. The events are then conducted stochastically using the kernels as probabilities for the transitions. Thus in this point-island limit the rate equations [Eq. (2.7)] are simulated exactly

with PCM [76]. There is no need to restrict PCM for point islands but then one must take into account geometric effects due to finite sizes of islands. One could calculate the kernels for example in the microscopic simulations and use them as input to PCM simulations [76]. It must be emphasized that PCM is not only related to island growth but it can be used to solve any problem where the rate equations are needed. Depending on the nature of the problem either PCM or numerical integration can be used.

The PCM simulations of island growth are carried out as follows. Let us first assume that the model concerns only aggregation events between islands. The system consists of a lattice with some distribution of islands. An island is chosen from the island list in the system and a random lattice site is chosen. If the final site is empty the island is moved into that site with uniform probability, otherwise one tests for an aggregation event with probability given by the kernel $K(i, j)$. If the aggregation event is accepted, a new island is formed with size $s = i + j$, otherwise islands are left in their original positions in the lattice. The fragmentation events can be accounted for as easily as aggregation. With fragmentation, an attempt is made to break the island. If this is not successful, an aggregation event is attempted as described above. The fragmentation event is successful with probability given by the fragmentation kernel $F(i, j)$. If the external particle flux is included, deposition events occur at the rate given by the flux parameter Φ such that at every Φ^{-1}th MC step a particle is deposited.

It must be emphasized that island jumps into empty lattice sites with equal probability are conducted only because of the MF assumption. Rate equations describe the system only in some average sense that applies to PCM, too. The MF approach is valid only if the spatial density of islands is uniform. In other words, in PCM the island lattice must be mixed enough so that on the average every island has non-zero probability to aggregate with any other island. If the jumps into empty sites are not introduced artificial correlations build up due to the incorrect implementation. It turns out, however, that the superfluous island hopping can be suppressed as will be discussed in the next Section.

Even if PCM is suitable strictly speaking only for simulating the system in the MF sense, one can mimic the effect of spatial correlations using different ways to choose aggregation and jump events [76]. Once the island is chosen the final site can be taken with the nearest neighbor (NN) or MF rule. With the NN rule one chooses the nearest neighbor site in the lattice and attempts an aggregation event or a jump if the site is empty. With the

MF rule any site in the lattice can be chosen. If there were any deviations between these two rules there would be deviations also in the real system due to spatial correlations between neighboring islands [76]. This would then mean that the spatial dimension is less than the upper critical dimension for the system. In larger dimensions spatial fluctuations can be neglected.

4.3 Revised particle coalescence method

As discussed above the MF assumption implicit in PCM requires that islands on the lattice must be mixed since the lattice itself does not represent any physical object. In practice the mixing can be implemented by allowing islands to jump into an empty lattice site with an equal probability. Implementing mixing in this way is straightforward but also time consuming. For example, in a 2D lattice with the system size $L^2 = 10^4$ and $N_{\mathrm{isl}} = 500$ islands the probability for an island to jump into an empty site instead of an aggregation attempt is $(L^2 - N_{\mathrm{isl}})/L^2 = 0.95$. This becomes even worse if the system size is increased since initially N_{isl} is very small.

Next we describe a new and fast method which improves the performance of PCM. These are unpublished results obtained by the author [1]. It was already realized in the original papers of PCM that picking an island from the island list, attempting the aggregation event with another island, and putting the resulting island (or islands) back to the list would be a good MF approach [76]. This could have been implemented e.g. with the simplified cluster-cluster aggregation model [82]. However, in this simplified picture the connection between physical time and simulation time step is not possible [76]. The mixing of the island list through island hopping was introduced in order to be able to study correctly the time dependence of the aggregation process [76], otherwise, for example, the dynamic exponent would be incorrect.

We adopt the notion that in the simulations the correct time step is not a constant but rather a stochastic variable in analog with the BKL method in Section 4.1. The BKL time becomes the same as the constant step on the average after many events. By introducing the variable time step the correct time development is obtained and there is no need for the actual lattice with islands and empty sites. One needs only the list of islands in the system and an imaginary system size L since the overall deposition rate depends on L.

In traditional MC the total transition rate is not known but a transition between configurations c and c' is performed with the probability $\nu_{c\to c'}/\nu_{\max}$ (see Section 4.1). It can be shown that in traditional Monte Carlo the correct time step can be drawn from the distribution given by Eq. (4.1) with Γ_c replaced by $\Gamma_M = N\nu_{\max}$ [83], where N is the number of all possible transitions in the system. In other words, at every step the physical time is incremented with Δt drawn from the correct distribution, no matter whether the transition attempt $c \to c'$ is successful or not.

This procedure can be easily generalized to include aggregation, fragmentation, and deposition. One has to count at every step all possible events for different processes which gives a transition rate for each process. Then, the total rate is given by $\Gamma_M = \Gamma_{\rm dep} + \Gamma_{\rm agg} + \Gamma_{\rm frag} = N_{\rm dep}\nu_{\max}^{\rm dep} + N_{\rm agg}\nu_{\max}^{\rm agg} + N_{\rm frag}\nu_{\max}^{\rm frag}$, where $N_{\rm dep}$ is the number of possible deposition events, and $\nu_{\max}^{\rm dep}$ is the corresponding maximum transition rate. $N_{\rm agg}$, $N_{\rm frag}$, $\nu_{\max}^{\rm agg}$, and $\nu_{\max}^{\rm frag}$ are the corresponding quantities for aggregation and fragmentation events. The event is randomly chosen according to the total rates of the event classes. One subtlety must be kept in mind, however. If the underlying lattice structure of the original PCM is removed deposition and fragmentation rates must be changed accordingly. This is due to the fact that jumps and aggregation events are grouped together where jumps correspond to waiting between two aggregation events. This leads in the new picture to *shorter* times between two fragmentation or deposition events. An obvious correction term is given by the number of empty sites removed from the system $L^2 - N_{\rm isl}$. Thus for each process one has the rates:

$$\begin{aligned} \Gamma_{\rm agg} &= 2K_0 N_{\rm isl}(N_{\rm isl}-1); \\ \Gamma_{\rm frag} &= \nu_{\max}^{\rm frag} N_{\rm isl}(L^2 - N_{\rm isl}); \\ \Gamma_{\rm dep} &= L^2 \frac{K_0}{\mathcal{R}}(L^2 - N_{\rm isl}), \end{aligned} \tag{4.2}$$

where K_0 is the prefactor of the aggregation kernel, $L^2K_0/\mathcal{R} = \Phi$ is the deposition rate, $\mathcal{R} = K_0/\Phi$, and $\nu_{\max}^{\rm frag}$ depends on the specific form of the fragmentation kernel. If the fragmentation kernel has the form $F(i+j=s) \propto s^\alpha(s-1)$ with $\alpha > -1$, then $\nu_{\max}^{\rm frag} = F(s_{\max})$, where $s_{\max}$ is the maximum island size in the system. Note that the correction term is included both in the fragmentation and deposition rates. Using the exact time steps and thus avoiding unnecessary island jumps needed to implement the MF approach makes the simulations faster even by a factor of 2000. With this improvement one can simulate at least five orders of magnitude in $\mathcal{R}$ whereas with the old PCM only two orders of magnitude is feasible.

5

Results

In this Chapter we provide some insight into the problems posed in the Introduction. New scaling relations in island growth in the case of the aggregation with fragmentation and deposition are presented followed by the results on the stability of circular islands. Then the meandering instability during step-flow is discussed and the selection of the meander wavelength and the invariant profile shape are demonstrated. At the end, coupling between island growth and meandering instability on vicinal surfaces is discussed.

5.1 Aggregation, fragmentation, and deposition

Generalizing the rate equations for aggregation to include fragmentation and deposition is straightforward. The final equation attains the form [31]:

$$\begin{aligned}\frac{\mathrm{d}n_s}{\mathrm{d}t} = \frac{1}{2}\sum_{i+j=s}\left[K(i,j)n_i n_j - F(i,j)n_{i+j}\right] \\ -\sum_{i=1}^{\infty}\left[K(i,s)n_i n_s - F(i,s)n_{i+s}\right] + \Phi\delta_{s,1}\end{aligned} \tag{5.1}$$

where $K(i,j)$ and $F(i,j)$ are the aggregation and fragmentation kernels, respectively, and Φ is the particle flux. The kernels are assumed to have homogeneous forms: $K(ai,aj) = a^{\lambda}K(i,j)$ and $F(ai,aj) = a^{\alpha}F(i,j)$, where $a > 0$ is a constant. The homogeneity exponents λ and α are the input parameters of the model together with the ratios $\mathcal{R} = K_0/\Phi$ and $\kappa = F_0/K_0$.

The scaling functions of the size distributions and the scaling properties of the mean size in aggregation with fragmentation suggest the scaling forms

(μ, α)	y	β	γ	δ	ψ_0
(2,0)	1/4	0.87	0.52	2.95	1.32
$(2, -\frac{1}{2})$	2/7	0.88	0.53	2.70	1.34
$(1, 0)$	1/3	1.12	0.63	1.95	1.50
$(1, -\frac{1}{2})$	2/5	1.13	0.59	1.55	1.63

Table 5.1. The scaling exponents y, β, γ, and δ and the constant ψ_0 as defined in the text. The exponent $y = 1/(\mu + \alpha + 2)$ is given by the MF relation. The analytical predictions are given by $\beta = 2/(1 + \mu)$, $\gamma = \beta/2$, and $\delta = 1 + \mu + \alpha$. Errors are ± 0.15 for β and γ, and ± 0.05 for δ.

also in the present case. The scaling exponents for the mean island size and the size distributions are derived in Appendix A together with the expression for the scaling function of the mean size. For the size distribution an ansatz of the form is proposed [31]:

$$g(x) = Ax^{\delta} \exp(-cx), \tag{5.2}$$

where A and c are constants and the scaling function $g(x)$ is related to the function $f(x)$ in Eq. (2.6) as $g(x) = xf(x)$. The task now is to determine the scaling exponents, in particular δ, since the size distribution specifies completely the problem once $\bar{s}$ is known.

In Publication I the scaling properties of the size distributions and the mean quantities have been simulated with PCM described in Section 4.2. The reaction kernels for aggregation and fragmentation were chosen to be [31]:

$$\begin{aligned} K(i,j) &= K_0 \varphi(i,j) = K_0 (i^{-\mu} + j^{-\mu}); \\ F(i,j) &= F_0 \phi(i,j) = F_0 (i+j)^{\alpha}, \end{aligned} \tag{5.3}$$

where the aggregation kernel takes the form $K(i,j) \propto D_i + D_j$ in two dimensions [36], and $D_i \propto i^{-\mu}$ is the diffusion coefficient of an island of size i. The form of the fragmentation kernel leads to the total fragmentation rate $F(s) = \sum_{i+j=s} F(i,j) \propto s^{\alpha}(s-1)$ [44]. Thus the aggregation and fragmentation kernels are homogeneous functions with the homogeneity exponents $\lambda = -\mu$ and α, respectively. In simulations we used the values $1 \leq \mu \leq 2$ which are reasonable choices for the island diffusion on metal surfaces [84, 85], and $-1/2 \leq \alpha \leq 0$, assumed to be reasonable in the case of ion-beam assisted deposition (IBAD) [86]. Other details are given in Publication I.

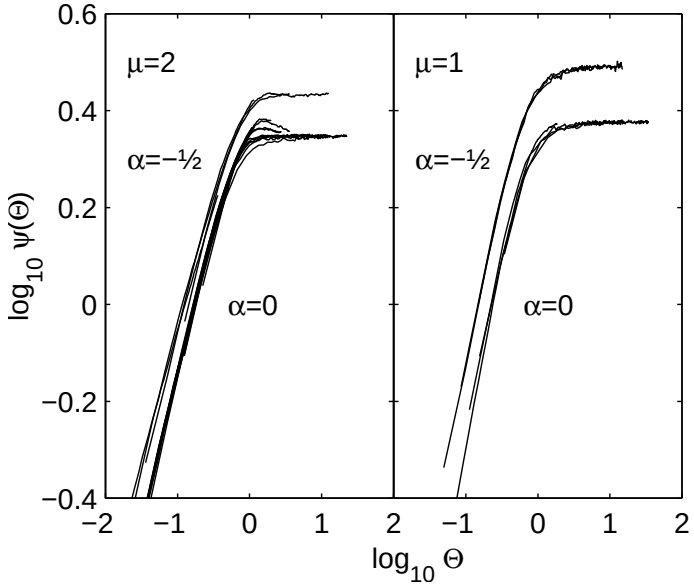

Figure 5.1. The scaling function for the mean size $\Psi(\Theta)$ [Eq. (A.8)] is displayed for the cases $(\mu, \alpha) = (2, 0)$, $(2, -\frac{1}{2})$, $(1, 0)$, and $(1, -\frac{1}{2})$ with the parameters $10^{-7} \leq \kappa \leq 10^{-5}$ and $0.5 \times 10^5 \leq \mathcal{R} \leq 2.0 \times 10^6$. The exponent β is measured from the slopes for $\Theta < 1$. In all cases the mean field exponent $y = 1/(\mu + \alpha + 2)$ for aggregation-fragmentation gives a good data collapse. Values for β and ψ_0 are reported in Table 5.1.

Simulation results for the scaling function for the mean island size confirm the scaling form proposed in Eq. (A.8). The scaling function is plotted in Fig. 5.1 as a function of the scaled coverage for various values of the homogeneity exponents and the parameters κ and $\mathcal{R}$. The scaling function behaves as a power-law for small argument values and approaches a constant at large values for all combinations of (μ, α), κ, and $\mathcal{R}$. Only at the cross-over region there are some deviations from the monotonic behavior for $(\mu, \alpha) = (2, 0)$. For the smallest values of κ the data points are in the power-law regime of the scaling function with the exponent β reported in Table 5.1. The measured values of β are larger than the result $\beta = 2/3$ obtained in the point-island approximation during irreversible growth [17]. The value of γ is consistent with models where adatom detachment occurs easily [15], but larger than MC simulation results with mobile islands where $\gamma \approx 0.4$ has been obtained [14, 87].

Figure 5.2 shows the limiting forms of the scaling function $g(x)$ for different values of the homogeneity exponents (μ, α). The solid lines are fits to the

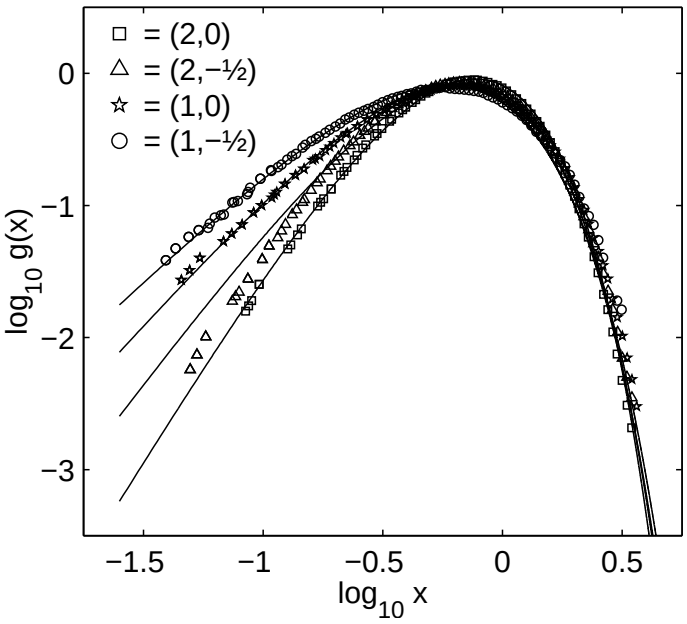

Figure 5.2. The scaling function $g(x)$ is shown with the homogeneity exponents (μ, α) indicated in the figure. The solid lines are fits to the function Eq. (5.2). For $x > 1$ the scaling function becomes independent of the input parameters of the model.

function Eq. (5.2). The scaling function has a distinctive behavior for $x < 1$ depending on both the μ and α exponents. For $x > 1$, however, the scaling function becomes independent of the homogeneity exponents, in addition to the parameters $\mathcal{R}$ and κ. Note that in Publication I it was anticipated that with deposition the value of δ should be smaller than without the flux. The exponent δ was ascribed to the value $\delta = 2 + \mu$ in the case of aggregation with fragmentation [47] which should read $\delta = 1 + \mu$. A more reasonable value $\delta = 1 + \mu + \alpha$ has been derived [48] which depends both homogeneity exponents, in agreement with Eq. (A.6).

To supplement Publication I we give some new results, including analytical predictions for the exponents $\beta = 2/(1 + \mu)$, $\gamma = \beta/2$, and $\delta = 1 + \mu - \alpha$ derived in Appendix A. The exponents β and γ reported in Publication I were afterwards found to deviate from the analytical predictions. However, the measured values for the exponents β and γ are consistent with Eq. (A.4). Both analytical and numerical values of β and γ increase as μ decreases, independently of α. The measured values for the exponent δ given in Table 5.1 and Eq. (A.6) are in good agreement, both depending on μ and α.

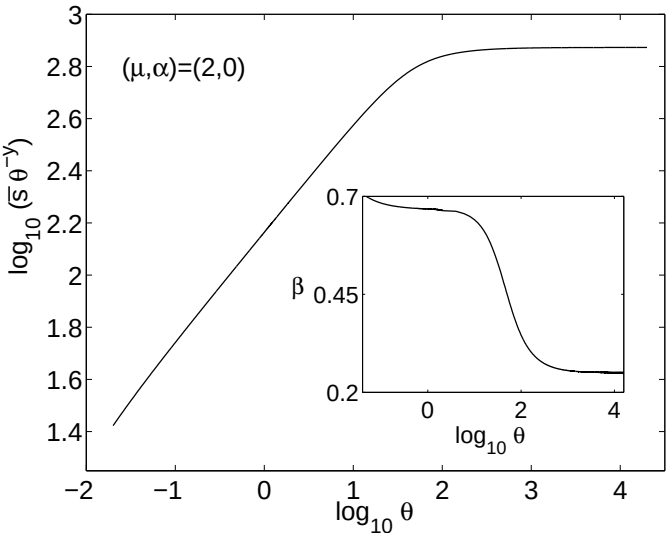

Figure 5.3. The numerical integration of Eq. (5.4) is shown for the case $(\mu, \alpha) = (2, 0)$. The mean size is scaled with $\bar{s} \sim \theta^y$ where $y = 1/4$ with these choices of the homogeneity exponents. The inset shows how the scaling exponent behaves as a function of coverage, starting from $\beta = 2/3$ and approaching $y = 1/4$. The units are arbitrary.

Deviations in β and γ can be attributed to the limited parameter range. Measuring the exponents roughly within a decade produces uncertainties to the values. This is confirmed by simulations using the revised PCM [1]. With the revised PCM much better averages and many orders of magnitude in parameters can be studied within a reasonable computation time. The measurements of β and γ with the revised method give the exponent values close to the analytical predictions. This is also confirmed by the numerical integration of the differential equation for the mean island size. It is obtained from the generalized Smoluchowski equation by multiplying Eq. (5.1) with s^2 and summing over s. This gives the equation for the second moment $M_2 \equiv \sum_s s^2 n_s$. The equation for $\bar{s}$ follows from the definition since $\mathrm{d}\bar{s}/\mathrm{d}t = (\mathrm{d}M_2/\mathrm{d}t - \Phi\bar{s})/\theta$, leading eventually to

$$\frac{\mathrm{d}(\theta\bar{s})}{\mathrm{d}\theta} = a\mathcal{R}\theta^{2-\lambda}(\theta\bar{s})^{\lambda} - b\kappa\theta^{-\alpha-1}(\theta\bar{s})^{\alpha+2} + 1, \tag{5.4}$$

where a and b are constants depending on the specific forms of the reaction kernels. The result of the integration in the case $(-\lambda, \alpha) = (2, 0)$ is shown in Fig. (5.3). The scaling assumption implies that at later times $\bar{s} \sim \theta^y$. Thus, by plotting $\bar{s}\theta^{-y}$ one obtains a straight line at later times, and a power law

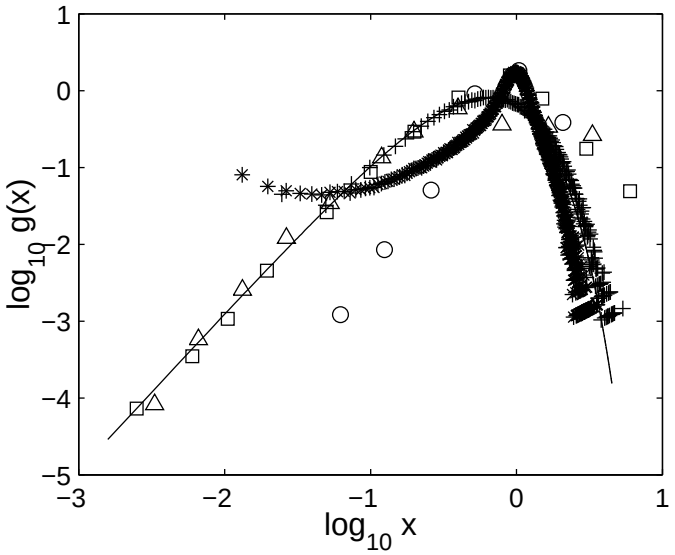

Figure 5.4. Scaled size distributions from IBAD experiments [8] with 400 eV ($\triangle$) and 4 keV ($\square$) Ar^+ ion energies are compared with vapor deposition ($\bigcirc$) [8], and the PCM results for $\kappa = 0$ with $\mu = 2$ ($*$), and for $\kappa = 10^{-5}$ with $(\mu, \alpha) = (1, 0)$ ($+$). The solid line is the scaling function for the latter case.

$\bar{s} \sim \theta^{\beta - y}$ at the onset. The inset shows the behavior of the scaling exponent of $\bar{s}$ in the semi-logarithmic scale. This is calculated through the logarithmic derivative $\mathrm{d} \log \bar{s} / \mathrm{d} \log \theta$. As can be seen from the figure, the exponent starts from the initial value $\beta \approx 0.65$ and approaches $\beta \approx 0.25$ in the final stage, in good agreement with the analytical values $\beta = 2/3$ and $\beta = y = 1/4$, respectively. Note that initially the regime of constant β is small, another possible origin for the deviations in the measured values.

We performed most of the simulations using both MF and NN aggregation and fragmentation rules (see Section 4.2). Using these different rules makes it possible to check the effect of spatial fluctuations [76]. It was found that only for the smallest fragmentation rates $\kappa < 10^{-7}$ were there deviations in the scaled size distributions, and for $\kappa \geq 10^{-6}$ all differences between MF and NN rules vanished. These findings were also checked by numerically integrating the rate equations in some representative cases and by performing independent MC simulations with a few parameter values. In all cases the data collapsed into the single curve, independent of the method. This suggests that spatial fluctuations have no effect whatsoever in aggregation with

fragmentation and deposition for the spatial dimensions $d \geq 2$. This implies that the upper critical dimension $d_c < 2$, i.e. in $d > d_c$ spatial fluctuations are not important, in accordance with aggregation and fragmentation [44]. In contrast, in aggregation d_c is a model dependent quantity given by $d_c = 2$ for the aggregation kernel used here [37, 88].

Finally we compare the PCM results with IBAD experiments. IBAD is a deposition technique where energetic ions are used during deposition to improve quality of growing layers. Using IBAD one can prevent formation of three-dimensional surface structures such that two-dimensional layer-by-layer growth prevails leading to improved smoothness of a surface [89]. During IBAD island growth is different from growth without ion bombardment. For example, the mean island size is smaller and the size distributions are broader than in thermal deposition [89] due to ion-enhanced adatom and island mobilities and island dissociation [10]. Fig. 5.4 shows a comparison between the scaled size distributions obtained from the PCM simulations [31, 90] and IBAD experiments [8]. For aggregation with deposition the size distribution function is highly peaked around the mean value and clearly differs from the experimental curve. However, the size distribution function for aggregation with fragmentation with the homogeneity exponents $(\mu, \alpha) = (1, 0)$ has qualitatively similar form to experimental results for ion bombardment. Only for large argument values there are deviations. These deviations might indicate coalescence of large islands during experiments which is not taken into account in PCM.

The results discussed above of island growth show that including fragmentation does change scaling of the size distributions and the mean island size. Moreover, the results clearly reveal that MF treatment is adequate and correlations do not play any role during growth when island fragmentation is included.

5.2 Bales-Zangwill instability in radial geometry

It is of interest to study the BZ instability in radial geometry, in particular in the case of circular islands and a crystalline cone. The cone consists of a stack of concentric islands acting as a prototype for a small circular nanostructure. Decay and bunching of such structures have been recently

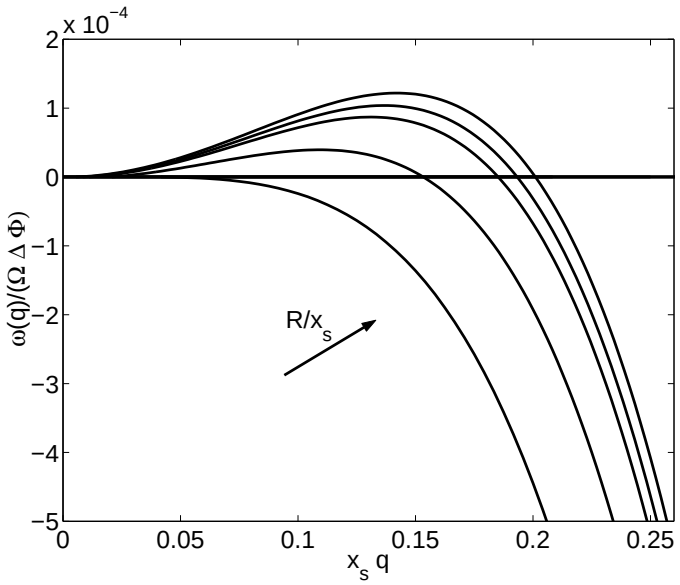

Figure 5.5. The growth rate $\omega(q)$ as a function of the wave number $q = n/R$ in the one-sided model. The radius of the step increases in the direction of the arrow. The stable regime corresponds to q for which $\omega(q) < 0$. All steps with $R < R_c$ are stable against meandering.

studied in detail [91] but only in the case of symmetric attachment from upper and lower terraces. Recently, experimental evidence of the meandering instability in radial geometry on Si(111) surfaces has been found [92].

The linear stability analysis of the BZ instability in radial geometry is reported in Publication II. The functional form of the growth rate ω of the perturbation in the most general case turns out to be complicated. In the following the results of the two cases are presented, viz. $k_+ \to \infty$, $k_- \to 0$ (one-sided model), and $k_+ \neq k_-$, both non-zero and finite (asymmetric model). It turns out that also in radial geometry the step edges can exhibit instability of diffusional origin in analogy to the BZ instability on a stepped surface. The details of the calculation of the growth rate of the instability are outlined in Appendix B.

Consider first the one-sided model. In Fig. 5.5 the growth rate in this case given by Eq. (B.3) is plotted against the wave number $q = n/R$ with various values of the radius R. It turns out that ω has a limiting form as R increases which is equivalent to decreasing curvature. From the figure, there exists a radius R_c such that all steps with $R < R_c$ are stable for all

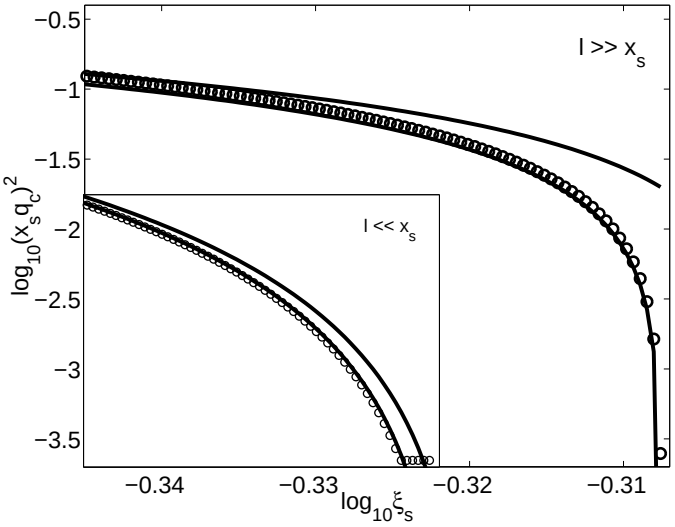

Figure 5.6. The critical wave number q_c is shown as a function of the capillary length ξ_s for the one-sided model. The circles are numerical values from Eq. (B.3), the upper curve is the BZ result, and the lower curve is Eq. (5.6) for $x_s q_c \ll 1$. The inset displays the case $L \ll x_s$. The corrected results follow rather well the full expression whereas the BZ curves deviate for large values of ξ_s.

q and steps with $R > R_c$ are unstable for perturbations $q < q_c$, where q_c is the critical wave number defined through $\omega(q_c) = 0$. The critical wave number depends on curvature such that q_c decreases with increasing κ. This means that the corresponding critical wavelength of instability changes to larger wavelengths. This is reasonable since the whole instability is due to competition between the line tension of the step edge and diffusional driving field from the terrace. For large curvatures the step edge is highly curved and small perturbations are smeared out by the line tension. For small curvatures the line tension does not have a significant effect and unstable growth with a band of wave numbers is possible.

For small curvatures it is possible to give analytical expressions for the growth rate, the critical radius, and the critical wave number in a few limiting cases. The small curvature is given by the limit $n, R \to \infty$ such that the ratio $q = n/R$ remains constant. The growth rate has the limiting form [93]:

$$\frac{\omega(q)}{\Omega\Delta\Phi} = \frac{\omega_{BZ}(q)}{\Omega\Delta\Phi} + \frac{x_s}{2R}\Sigma_q, \tag{5.5}$$

where ω_{BZ} is the BZ expression [19], and

$$\begin{aligned}\Sigma_q = &-\left[2+L^2q^2\right]\tanh(L)+\left[L^2q^2+\Lambda_q^{-2}\right]\tanh^2(\Lambda_q L)\tanh(L)\\ &+\left\{x_sLq^2\Lambda_q^{-2}+\Lambda_q^{-1}[L^2q^2+\Lambda_q^{-2}]\tanh(\Lambda_qL)\right.\\ &\qquad\left.+\tanh(L)-2\xi_s\right\}/\cosh(\Lambda_qL)\cosh(L)\\ &+2\xi_s+\xi_sx_s^2L^2q^4-\xi_sx_sq^2[L^2q^2+\Lambda_q^{-2}]\tanh^2(\Lambda_qL),\end{aligned}$$

where $\Lambda_q=\sqrt{1+(x_sq)^2}$, L is the terrace width, and all function arguments have been scaled with x_s. Using this form one can determine the critical wave number in the limiting cases. For $L \gg x_s$ we have [93]:

$$x_sq_c=\begin{cases}\sqrt{\frac{1}{\xi_s}-\frac{x_s}{R}(2-\xi_s^{-1})}, & x_sq_c\gg 1;\\ \sqrt{\frac{4}{3}(1-2\xi_s)-\frac{2x_s}{R}}, & x_sq_c\ll 1.\end{cases} \tag{5.6a}$$

For $L \ll x_s$ (and $L^2q_c^2 \ll 1$) we have [93]:

$$x_sq_c=\sqrt{\frac{L}{2x_s\xi_s}-1-\frac{L}{R}}. \tag{5.6b}$$

As $R\to\infty$ the results approach the BZ expressions [see Eqs. (3.8)]. Using these expressions one can define the critical radius R_c such that steps with $R<R_c$ are stable. In the long-wavelength limit $q_c\approx 0$ one obtains:

$$R_c=\begin{cases}\frac{3x_s}{2(1-2\xi_s)}, & L\gg x_s \quad (x_sq_c\ll 1);\\ \frac{2\xi_sL}{L-2\xi_s}, & L\ll x_s \quad (L^2q_c^2\ll 1).\end{cases}$$

In radial geometry instability is suppressed by curvature and the step edges smaller than the critical radius R_c are always stable against meandering. As can be seen above, R_c depends on the microscopic parameters in the system, e.g. diffusion coefficient, driving force, and the line tension of the edge.

In Fig. 5.6 the asymptotic results for q_c are compared with the BZ expression as a function of the capillary length in the case $L \gg x_s$, $x_sq_c \ll 1$. The results with $1/R$ corrections follow the full expression while the BZ results have deviations for large values of ξ_s. As ξ_s increases q_c approaches zero and for large enough values of ξ_s the step edge is always stable. In the inset the case $L \ll x_s$ is shown which has a similar behavior.

The complete expression for the growth rate with an arbitrary phase difference between adjacent steps in the asymmetric case is rather complicated.

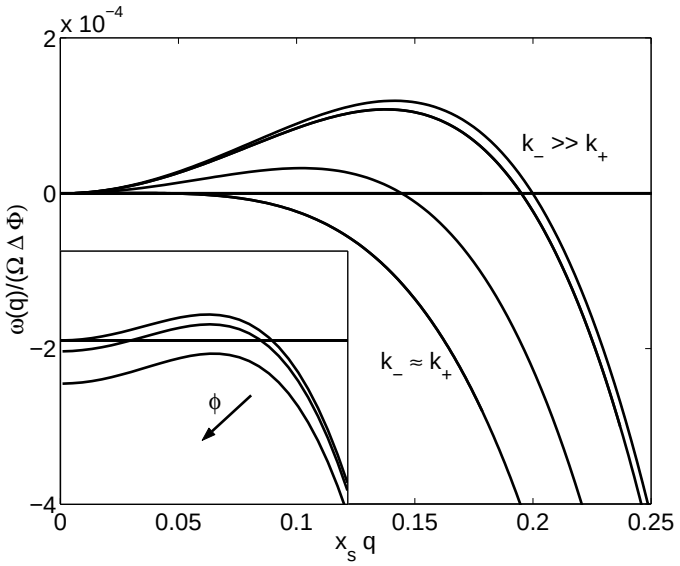

Figure 5.7. The growth rate ω as a function of the wave number for different values of the sticking coefficients k_+ (from below) and k_- (from above). If $k_- \leq k_+$ the steps are always stable. The inset displays the effect of the phase difference of the perturbations between adjacent steps.

However, numerically it behaves in a similar way as the one-sided case. In Fig. 5.7 the numerical values of the general expression for ω are shown in the asymmetric model. It is found that when the sticking coefficients approach each other the edge becomes stable against meandering. This implies that the one-sided model is the most unstable one as in the case of rectangular steps [19]. The phase-difference ϕ of the perturbations between the adjacent step edges introduces one degree of freedom. The plotted growth rates are shown in the inset of Fig. 5.7. The results show that the in-phase mode where adjacent steps have perturbations in the same phase is the most unstable growth mode. This is also the case in the rectangular geometry [94].

In radial geometry the sizes of unstable circular steps turned out to be large. It also seems that the time scale for the evolution of the meandering instability is rather large compared with the advancement of the steps in radial geometry being of the order of seconds [92]. Thus island morphology is rather stable, in particular on vicinal surfaces, in the time and length scales of interest.

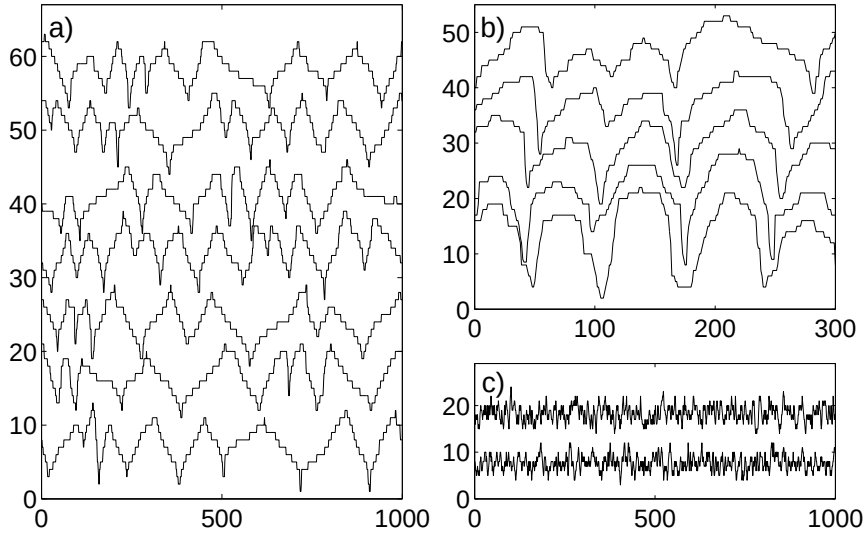

Figure 5.8. Snapshots of step profiles at $T = 240$ K with $\Phi = 6 \times 10^{-3}$ ML/s with close-packed step edges in (a) and (b), and open step edges in (c). In the last case KESE stabilizes the step edge. Coverage is $\theta = 1.0$ ML in (a), $\theta = 5.0$ in (b), and $\theta = 4.0$ in (c). Horizontal and vertical scales are given in the units of the lattice constant.

5.3 Kink Ehrlich-Schwoebel effect

Next we consider the meandering instability of step edges caused by the kink Ehrlich-Schwoebel effect (KESE) [20]. The wavelength selection of the meandering and an invariant meander shape are discussed. The results demonstrate the emergence of a new length scale and the importance of step instabilities during growth.

5.3.1 Wavelength selection

The BZ instability is basically due to asymmetric mass currents onto the step edge from the upper and lower terraces. This asymmetry has in many cases its origin in the ES barrier at the step edge. Recently it has been proposed that an analogous situation may arise also in one dimension where the barrier is denoted as the kink ES barrier [20]. This barrier suppresses adatoms for going around the kink sites at the step edge. The corresponding kink ES effect (KESE) leads to growth of an instability at the step edge

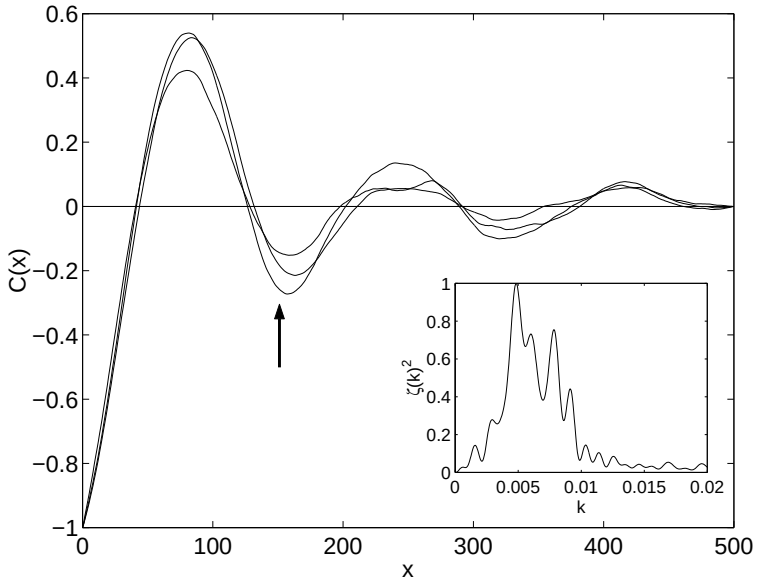

Figure 5.9. The spatial correlation function of the step profiles $C(x)$ is shown along the close-packed direction for coverages $\theta = 0.1$, 1.0, and 2.0 ML at $T = 270$ K and $\Phi = 6 \times 10^{-3}$ ML/s. The arrow denotes the wavelength obtained by calculating the average separation of the meanders. The inset shows the corresponding Fourier modes of the squared step profiles.

with a dynamically selected wavelength [20]. In following the results of Monte Carlo simulations using the BKL algorithm explained in Section 4.1 are presented. These results with the simulation details are reported in Publication III.

Fig. 5.8 displays snapshots of the step profiles for a few coverages. The formation of structures is evident. At the onset the unstable patterns develop independently at the adjacent steps and begin to phase-lock at the largest coverages studied. However, the formation of unstable patterns happens only at the close-packed steps. For the open step edges there are no evidence of periodic structures as shown in Fig 5.8 (c). This is in contrast to recent experiments where unstable patterns have been observed during growth of vicinal Cu surfaces with both close-packed and open step edges [63]. Qualitatively, KESE should stabilize the open step edges since clearly the particle currents at the edge are towards the step. This implies that protrusions at the open edge are only small fluctuations around the average position. Thus the origin of the meandering instability at open step edges remains an open question. A possible explanation could be that

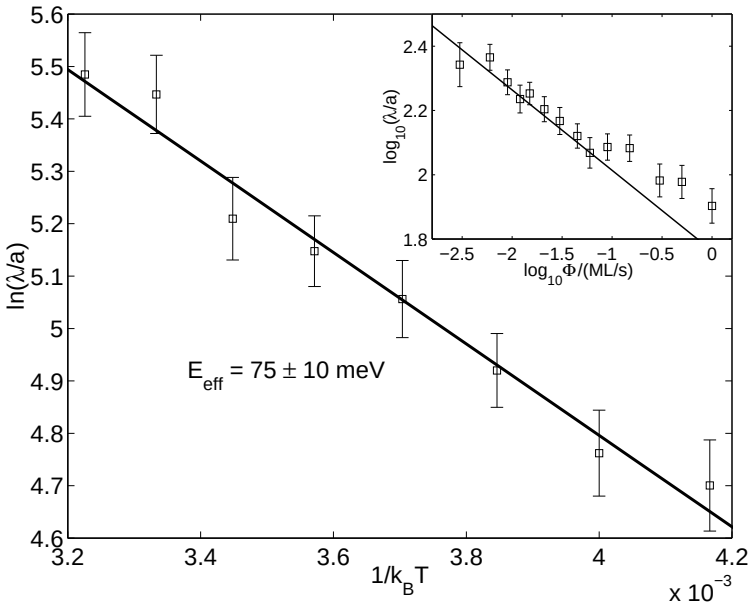

Figure 5.10. Temperature dependence of the meander wavelength λ is shown in an Arrhenius plot at $\theta = 2.0$ ML with $\Phi = 6 \times 10^{-3}$ ML/s at temperatures $T = 240 - 310$ K. The solid line is the least squares fit to the data points with a slope given in the figure. The inset shows the flux dependence of λ on a log-log scale at $\theta = 2.0$ ML, $T = 300$ K with $\Phi = 3 \times 10^{-3} - 1.0$ ML/s. The solid line is the prediction for λ based on the dimer nucleation length.

impurities (S on Cu surfaces) attach irreversibly to open step edges and act as a pinning centers for growing fluctuations. Another cause could be strain effects at open steps which would influence the energy barriers and the relative importance of the microscopic processes at the open edges.

To quantify the unstable wavelength one can extract the step edge profiles and count the number of wave crests. Another method is to use a correlation function of the step profiles. If the profiles have any periodicity the spatial correlation function should have it, too. The step profile correlation function is defined as:

$$C(x) = \langle \zeta(x + x_0)\zeta(x_0) \rangle, \tag{5.7}$$

where $\zeta(x) = h(x) - \bar{h}$, $h(x)$ is the step profile, and $\bar{h}$ is the average profile. The brackets denote averages over noise and all steps in the system. The correlation function is shown in Fig. 5.9 at different coverages. It can be seen that $C(x)$ is rather independent of coverage indicating that the

structures saturate at the early stage of growth. The periodic structure is revealed through the periodicity of $C(x)$. The arrow denotes the value of the wavelength measured by counting the number of unstable structures at the edge. In the inset the Fourier transform of the squared step profiles is shown. There are many different Fourier modes contributing to the profile shape, the dominant one close to $2\pi/\lambda$. The myriad of Fourier modes is due to irregular shape and front-back asymmetry of the step profiles. Only for a perfect periodic sinusoidal shape the Fourier spectra would have a single sharp peak.

The length scale extracted from the correlation function data can be compared with the analytical prediction for the wavelength of unstable structures. Assuming that dimers are stable at the step edge leads to the form [73, 95]:

$$\lambda \approx \frac{1}{2}\left(\frac{12D_s}{\Phi_s}\right)^{1/4},$$

where $D_s \propto \exp(-E_d/k_BT)$ is the diffusion coefficient along the straight edge, E_d is the corresponding diffusion barrier, and $\Phi_s = \Phi L$ is the flux onto the edge. This form predicts that the temperature dependence of λ has an effective barrier $E_{\text{eff}} = E_d/4$, and the flux dependence has the exponent $-1/4$. The BZ prediction would give a larger barrier and $\Phi^{-1/2}$. In Fig. 5.10 the temperature dependence of λ is shown in an Arrhenius plot. The effective barrier extracted from the data gives $E_{\text{eff}} \approx 75$ meV, in agreement with the predicted value $E_d/4 = 65$ meV based on the energy parameters of the model. The inset shows the flux dependence plotted together with the predicted curve on a log-log scale. The data follow rather well the expected $\Phi^{-1/4}$ line. Only for the largest fluxes there are some deviations, probably due to island nucleation on terraces. Fitting the power law to the data points up to $\Phi = 0.1$ ML/s gives $\Phi^{-0.23}$, in agreement with the expected power-law. These results are in good agreement with the recent experiments [63].

5.3.2 Shape of step profiles

The average shape of the unstable step patterns is also an interesting issue since it can provide information on microscopic processes contributing to the formation of instability. The results of Publication III had some evidence of phase-locking of the growing unstable structures on step edges for large

coverages. Previous MC simulations with the simplified SOS model have shown that a triangular shape is expected for strong KESE but a rounded shape should be obtained for weak KESE in the case of an isolated step [20]. The simulation results reported in Publication III, however, are in disagreement with that conclusion. For strong KESE it was found that at the onset of growth the profiles have a triangular shape which changes to more rounded form as coverage increases [96]. In the following the profile shapes are discussed based on Publication IV.

Fig. 5.11 shows the scaled average profile shapes calculated at $\theta = 0.2$, 1.0, and 3.0 ML at $T = 300$ K with $\Phi = 8 \times 10^{-2}$ ML/s. The average shape has been obtained from the complete profiles by identifying the meanders $\zeta(x, \theta)$ (see Fig. 5.8), averaging over them, and scaling the average meander by the width w defined as $w^2(\theta) = \langle \zeta(x, \theta)^2 \rangle$. As coverage increases the scaled average profile approaches a limiting shape which is independent of θ. The shape also seems to become more rounded as θ increases. The inset shows the same profiles without scaling with the width.

Quantitatively, the approach towards an invariant shape can be studied by considering the nth lateral moments of the profiles. The moments are defined through

$$M_n(\theta) = \langle \zeta(x, \theta) x^n \rangle \ . \tag{5.8}$$

For example, M_2 is the area of the parabola weighted with the profile. In Fig. 5.12 (a) the even moments up to $n = 10$ are shown as a function of coverage on a semi-logarithmic scale. It can be seen that the moments saturate around $\theta = 1.0$ ML indicating that the profile shape also saturates at the same coverage. This is interesting since the width of the profiles does not show any sign of saturation up to $\theta = 10.0$ ML. Moreover, $w \propto \theta^{0.3}$ which is in contrast to numerical integration of the continuum step equations where $w \propto \theta^{1/2}$ has been found [61]. In addition, recent SOS simulations indicate that $w \propto \theta$ in the case of the BZ instability and saturation of w in the case of KESE [66]. However, a small coverage regime in our simulations cannot be used to conclusively determine the value of the width exponent of the profiles. If anything, there might be a transient regime up to tens of monolayers before the power-law or saturation regime can be reached.

The results indicate that the average meander shape obtained from the simulations and the corresponding lateral moments are rather insensitive to the parameters of the system, viz. temperature and flux [97]. This implies that the invariant profile shape is independent of the microscopic diffusion

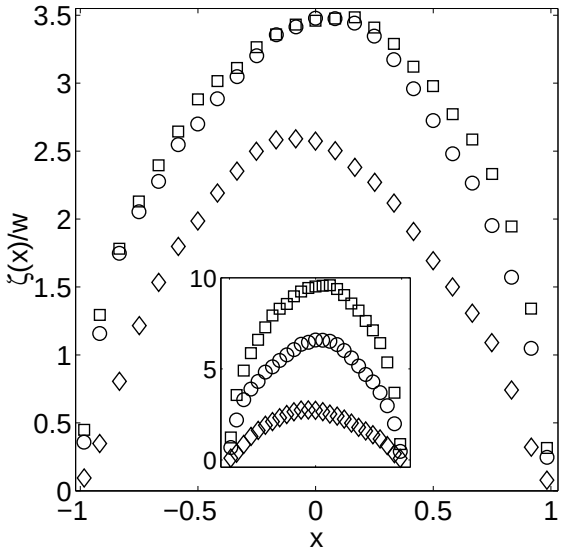

Figure 5.11. The scaled average meander profile $\zeta(x)/w$ is shown at $T = 300$ K for $\Phi = 8 \times 10^{-2}$ ML/s at $\theta = 0.2$ ML ($\diamond$), $\theta = 1.0$ ML ($\bigcirc$), and $\theta = 3.0$ ML ($\square$). The inset shows the average meanders without scaling.

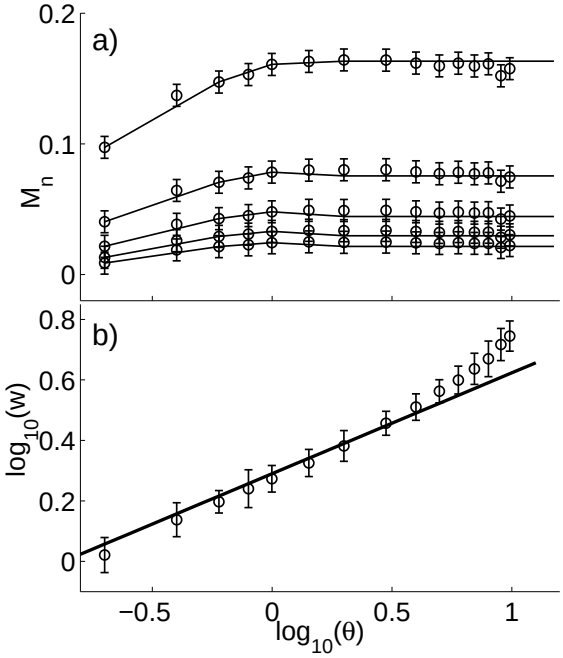

Figure 5.12. (a) The even lateral moments M_n (from $n = 2$ up to $n = 10$ from top to bottom) are displayed as a function of coverage on a semi-logarithmic scale. (b) The width w of the step profiles as a function of coverage behaves as $w \propto \theta^{0.3}$ up to $\theta = 5.0$ ML.

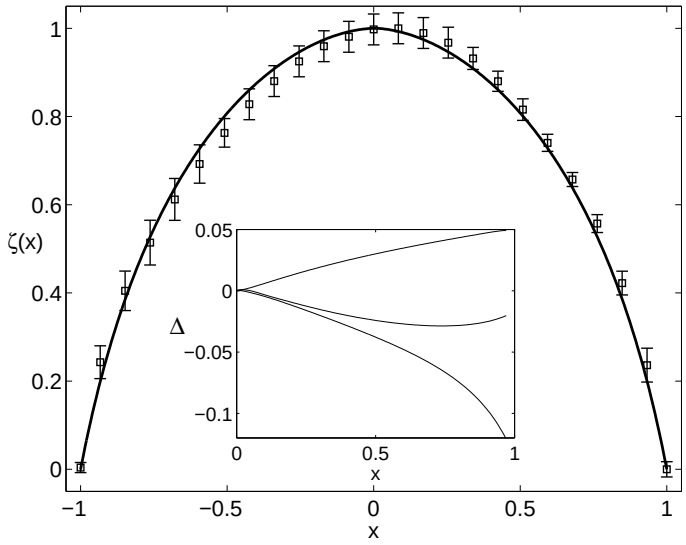

Figure 5.13. The average pattern shape is shown at $T = 300$ K, $\theta = 8.0$ ML with $\Phi = 6 \times 10^{-2}$ ML/s (□). The solid line is the profile obtained from the integration of the stationary continuum equation. The inset shows differences in the profiles $\Delta = [\zeta_{\mathrm{all}} - \zeta_i]/\zeta_{\mathrm{all}}$, where ζ_{all} is the profile with all currents included, and ζ_i $(i = k, e, SB)$ denotes the current where only a small contribution from J_i is included in the integration.

processes at the step edge. The invariance of the profiles can be explained by the geometric constraints in the phase-locking regime where the steps advance at the same velocity at the same positions. This assumption can be checked by comparing the simulation profiles with the profiles obtained by the integration of the continuum step equations in the stationary limit. The step edge obeys a dynamic equation [61, 72, 73]:

$$\frac{\partial \zeta}{\partial t} = -\frac{\partial J_{\mathrm{tot}}}{\partial x},$$

where $J_{\mathrm{tot}} = J_k + J_e + J_d + J_{SB}$, and the partial currents are given by Eqs. (3.11)–(3.14). It should be noted that solving numerically the full dynamic equation is a non-trivial task even without the KESE current [61,74]. Therefore, we concentrate on a stationary regime where $\partial_t \zeta = 0$. In this limit one solves $m(x) = (\partial_x \zeta)/\sqrt{1 + (\partial_x \zeta)^2}$ from the equation $J_{\mathrm{tot}} = 0$. When $m(x)$ has been determined the meander profile ζ can be obtained by numerically integrating $\partial_x \zeta = m(x)/\sqrt{1 - m(x)^2}$. For boundary conditions one uses m_0 such that the integration is performed within the interval

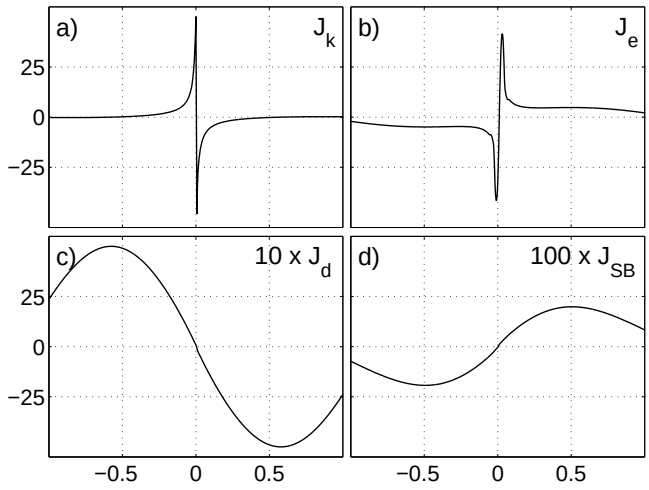

Figure 5.14. The partial mass currents Eqs. (3.11)–(3.14) are shown where integrated profile is used as an input. Note that in (c) and (d) the currents are multiplied with factors 10 and 100, respectively.

$-m_0 \leq m(x) \leq m_0$. The value $m_0 \approx 0.97$ is consistent with the slope of the simulation profile.

In Fig. 5.13 the simulation profiles are compared with the solution to the stationary continuum equation. In agreement with the simulations the shapes are insensitive to the parameters T and Φ as long as they vary in sensible limits. The inset shows the relative differences between the complete solution and those solutions where one of the partial currents is artificially made small.

The mass currents (3.11)–(3.14) are shown in Fig. 5.14 where the integrated profile is used as an input. The partial currents J_k and J_e have the largest contribution close to the origin whereas J_d dominates close to end points. The curves suggest that there is a delicate balance between the mass currents, the Gibbs-Thomson current J_e compensated by the sum of other terms. It must be emphasized that the compensation is effective only for the invariant shape. Since the currents are extremely sensitive to the specific form of the average profile, one cannot make conclusions using for example a square shape as an input.

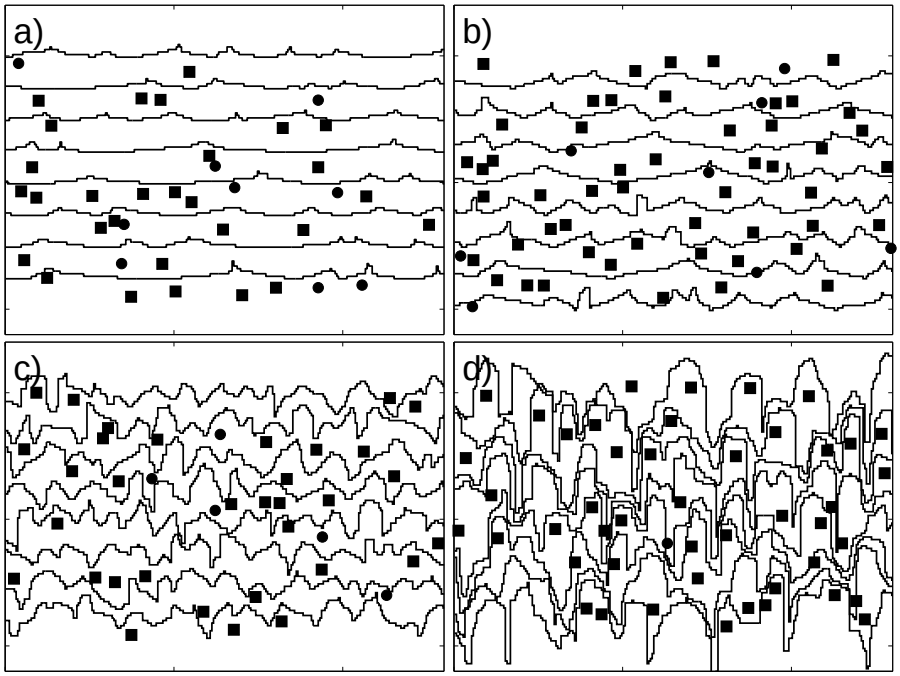

Figure 5.15. Snapshots of surface configurations are shown on fcc(1,1,25) surface at $T = 240$ K, $\Phi = 0.1$ ML/s, and coverages (a) 0.1 ML, (b) 0.3 ML, (c) 2.0ML, and (d) 10.0 ML. The solid lines are the single-valued step profiles and the black squares denote the center-of-mass positions of terrace islands. The axes range up to 250 in the horizontal and 125 in the vertical directions in the units of the lattice constant.

5.4 Mixing island growth and kink Ehrlich-Schwoebel effect

In any real growth problem there are usually both pre-existing steps and islands on a surface. Complications arise from the fact that both island growth and step flow have their own characteristic length scales. On stepped surfaces where KESE is operative the characteristic scale develops on step edges as periodic meanders form [20,63,66,96]. On flat surfaces the scale can be associated to the average distance between growing islands [16,17]. One expects a non-trivial behavior of these scales when islands form on a vicinal surface since the lengths have different scaling behaviors as a function of D/Φ. Publication V is an attempt to bridge the gap between these growth modes using BKL simulations on vicinal surfaces [98].

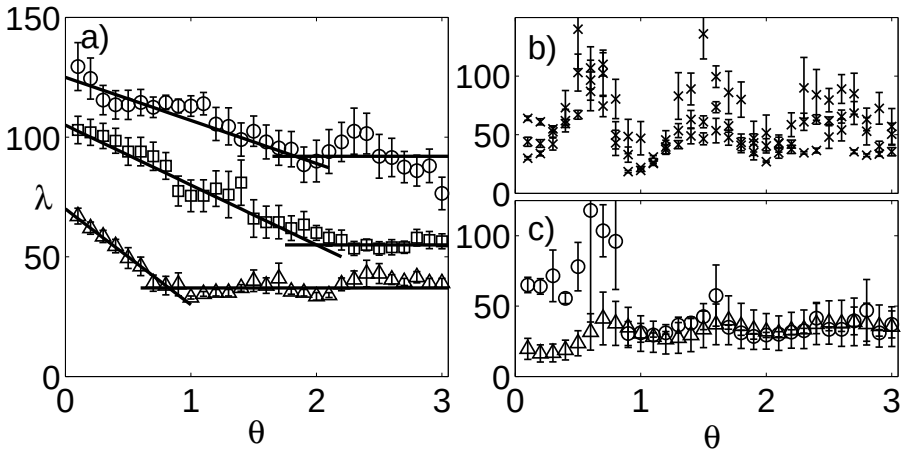

Figure 5.16. (a) The meander wavelength λ as a function of coverage at $T = 240$ K for $\Phi = 0.05$, 0.1, and 0.5 ML/s from top to bottom. (b) λ as a function of coverage at $T = 200$, 220, and 240 K for $\Phi = 1.0$ ML/s. (c) λ ($\bigcirc$) and the island separation $(NL)^{-1}$ ($\triangle$) as functions of coverage at $T = 240$ K for $\Phi = 0.75$ ML/s.

In Fig. 5.15 the snapshots of the fcc vicinal surface are shown in the case where island formation on terraces take place. The parameters are $T = 240$ K, $\Phi = 0.5$ ML/s, and the terrace width $L = 12.5a$, where a is the lattice constant, at coverages (a) $\theta = 0.1$ ML, (b) $\theta = 0.3$ ML, (c) $\theta = 2.0$ ML, and (d) $\theta = 10.0$ ML. From the figure it can be seen that at small coverages steps meander and islands nucleate rather independently whereas at large coverages islands and steps begin to coalesce leading to complicated interplay between two growth modes. Islands attach to step edges due to coalescence changing step morphology to complicated step profiles. The step edge locally advances abruptly ahead if an island attaching to the edge is large. These protrusions relax rather quickly such that the step profiles attain the single-valued shape. For the highest fluxes, however, the relaxation is not fast enough and vacancy islands are nucleated on terraces.

The changing and coupling of length scales are demonstrated in Fig. 5.16. In Fig. 5.16 (a) it is shown how the meander wavelength λ behaves as a function of coverage for fluxes $\Phi = 0.05$, 0.1, and 0.5 ML/s (from top to bottom). In all cases λ gradually decreases until it reaches a saturation value depending on the flux. The approach to the saturation value depends on the flux, too, such that for small fluxes the saturation takes place at larger coverages. When the flux increases or temperature decreases one observes

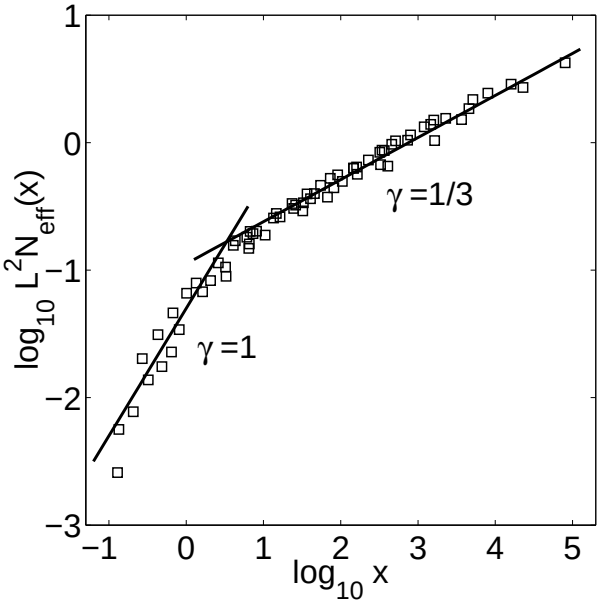

Figure 5.17. The scaled effective island density $L^2 N_{\text{eff}}$ is shown as a function of $x = \theta\Phi/\Phi_c$, where $\Phi_c = D/L^6$ for various values of L and $\theta \leq 0.3$ ML. The scaling of N_{eff} implies that $N_{\text{eff}} \propto x^{\gamma}$, where the value of the scaling exponent γ depends on the regime.

a saturation regime. This is shown in Fig. 5.16 (b) where λ is plotted at temperatures $T = 200$, 220, and 240 K for $\Phi = 1.0$ ML/s. In all cases the wavelength oscillates around the common mean value. This is probably due to complicated step edge profiles which are no longer single-valued curves. This can lead to an erroneous determination of the exact value of λ through the correlation function. However, the oscillations might indicate alternating step-flow and island formation. Oscillations of reflection high energy electron diffraction (RHEED) have been observed in layer-by-layer growth originating from oscillations in step densities [11]. For a complete layer one has minimum number of steps and minimum of RHEED intensity whereas maxima are obtained when the number of islands on terraces has the maximum value.

For small terraces island nucleation is dominated by the steps since many adatoms attach to step edges instead of nucleating new terrace islands. Quantitatively, one can use arguments of Refs. [27, 72] to derive the scaling

form for N on a vicinal surface. The island density becomes [98]:

$$L^2 N_{\text{eff}} \sim \begin{cases} f, & f \ll 1; \\ f^{1/3}, & f \gg 1, \end{cases} \tag{5.9}$$

where $f = \theta\Phi/\Phi_c$, and the two regimes correspond to small and large terraces, respectively. Details can be found in Publication V. Fig. 5.17 displays the scaled island density in the submonolayer regime. As can be seen from the figure, at small argument values step-dominated scaling is valid and for large x scaling for singular surface applies. This confirms that in the submonolayer regime island separation and step-flow are independent.

6

Summary and discussion

This thesis consists of studies related to pattern formation during surface growth. The aim was to bridge the gap between traditional approaches where island growth and step-flow are treated as separate growth modes. Surface growth by molecular beam epitaxy (MBE) is rather limited in parameter ranges for smooth layer-by-layer growth and other techniques must be utilize to improve the quality of growing layers, e.g., for large external fluxes. The other methods, however, induce new processes to the simple MBE picture such as island mobility and fragmentation, and consequently, new scaling relations and length scales. Towards this end, we concentrated on some important aspects of surface growth, namely island growth with aggregation, fragmentation, and deposition, stability of circular islands, meandering instability during step-flow, and coupling between island formation and step meandering.

In island growth, motivated by the ion-beam assisted deposition experiments, aggregation with fragmentation and deposition were examined. The scaling forms for the size distributions and the mean island size were proposed and their validity confirmed with the simulations using the particle coalescence method (PCM). Correlations between island separations and sizes were shown to disappear due to island fragmentation. Additional results supplementing the published ones were provided, in particular, analytical estimates for the scaling exponents and the new improved version of PCM. By numerical integration the analytical values for the scaling exponents of the mean island size were confirmed.

Stability of circular steps was analytically studied in the spirit of the Bales-Zangwill (BZ) instability. Correction terms to the BZ results were derived in the limit of the large step radius, such as the critical values for the wave number of the unstable growth modes. A criterion for the critical step radius was derived in the limit of long wavelengths. The results extend

the BZ findings from rectangular to radial geometry and demonstrate that rather large length and time scales are needed to observe the meandering instability in radial geometry.

On vicinal surfaces stability of steps was examined with Monte Carlo simulations. At close-packed step edges meandering is caused by the kink Ehrlich-Schwoebel effect instead of the BZ mechanism. The wavelength selection and its scaling with respect to the deposition flux and temperature were demonstrated, in agreement with recent experiments. The shape of the average meander profile extracted from the simulation data attain an invariant shape. This was compared with the integration of the continuum step equation in the stationary limit. Both the continuum and simulation profiles were insensitive to the model parameters.

Finally, simulations on vicinal surfaces were performed in conditions where islands nucleate on terraces and step edges exhibit meandering instability. In the submonolayer regime these two growth modes were found to be independent. After islands begin to coalesce with the step edges the coupling between the island separation and step meandering emerges. The mixing length scales were demonstrated to lead to an interesting growth mode with a new length scale different from the original ones.

The results are of importance in constructing more realistic models of surface growth. Several issues remain unresolved, though. It is plausible that only single atoms can detach from islands, a realistic situation in island growth. This leads to different homogeneity properties of the fragmentation kernel and possibly has consequences on scaling of the size distributions and the mean island size. In step-flow growth, the origin of the observed value of the exponent for the step profile width remains a puzzle as well as meandering at open step edges. Also the scaling properties of the new length scale in the case of coupling between island growth and step-flow deserves a closer study. It seems likely that a full dynamic information of step-flow can be probably obtained only through the continuum modeling. A reasonable attempt would be to take nucleation into account in rate equations in two dimensions in a realistic way. Another promising candidate could be based on a phase-field approach [99]. Work in these directions is in progress.

Appendix A

Derivation of the scaling exponents

Here the scaling exponents for the mean island size and the size distribution function are derived followed by the scaling function for the mean size. To determine the scaling exponents, take the continuum limit $s, i, \bar{s} \to \infty$, $s/\bar{s} = const.$ in Eq. (5.1), insert the scaling ansatz Eq. (2.6), and assume that the integrals converge at both limits. This gives

$$\frac{1}{\bar{s}^2} f(x) - \frac{\theta \dot{\bar{s}}}{\bar{s}^3} \left[2f(x) - xf'(x)\right] = \frac{1}{2}\theta^2 \bar{s}^{\lambda-3} \mathcal{R} G_1(x) - \theta \bar{s}^{\alpha-1} \kappa G_2(x), \quad \text{(A.1)}$$

where $\dot{\bar{s}}$ is the derivative with respect to θ, $f'(x) = \mathrm{d}f/\mathrm{d}x$, $x = s/\bar{s}$, $\mathcal{R} = K_0/\Phi$, and $\kappa = F_0/\Phi$. Note that the deposition term vanishes in the continuum limit, and the only effect of deposition is to increase θ. The functions $G_{1,2}(x)$ are given by

$$\begin{aligned} G_1(x) &= \frac{1}{2}\int_0^x \mathrm{d}y K(y, x-y) f(y) f(x-y) - f(x) \int_0^\infty \mathrm{d}y K(x,y) f(y); \\ G_2(x) &= \frac{1}{2}\int_0^x \mathrm{d}y F(y, x-y) f(x) - \int_0^\infty \mathrm{d}y F(x,y) f(x+y). \end{aligned} \quad \text{(A.2)}$$

There are two limits we are interested in. Physically, at the onset of growth the fragmentation term is negligible, and we are left with the expression

$$\bar{s} f(x) - 2\theta \dot{\bar{s}} f(x) - \theta \dot{\bar{s}} x f'(x) = \theta^2 \bar{s}^\lambda \frac{\mathcal{R}}{2} G_1(x). \quad \text{(A.3)}$$

The only way that the coverage and x dependence can be separated is that $\bar{s}$ follows a power law. This implies that $\bar{s} = \theta^2\ \mathcal{R}\bar{s}^\lambda$, from which it follows

that $\bar{s} \sim \mathcal{R}^{\gamma}\theta^{\beta}$, with the scaling exponents

$$\begin{aligned} \gamma &= \frac{1}{2}\beta; \\ \beta &= \frac{2}{1-\lambda}. \end{aligned} \tag{A.4}$$

These are in contrast to pure aggregation where $\beta = z = 1/(1-\lambda)$, and to aggregation with fragmentation where $\beta = y$. The exponent γ is not defined in either of these cases since $\Phi = 0$. In irreversible growth where islands grow only by attachment of adatoms during growth one has $\beta = 1$ and $\gamma = 2/3$ [17] ($\beta = 2/3$ in point-island approximation [16]).

The scaling exponent δ for the size distribution function follows through the x dependence of Eq. (A.1): $G_1(x) = G_2(x)$. We insert Eq. (5.2) into the relation between $G_{1,2}(x)$ with $f(x) = x^{-1}g(x)$ which gives

$$\begin{aligned} G_1(x) &= C_1 \mathrm{e}^{-x}\ x^{\lambda+2\delta-1}; \\ G_2(x) &= C_2 \mathrm{e}^{-x}\ x^{\delta+\alpha}, \end{aligned} \tag{A.5}$$

where C_1 and C_2 are constants depending on the explicit form of the reaction kernels. Equating the powers of x of these expressions gives

$$\delta = -\lambda + \alpha + 1. \tag{A.6}$$

The same result is found also in aggregation with fragmentation [47].

At later times fragmentation becomes important and one presumably has a quasi-stationary state where only θ increases. Thus the time derivative of the size distribution vanishes [left hand side of Eq. (A.1)] and we get similar to fragmentation that $\bar{s} \sim \kappa^{-y}\theta^{y}$ with the scaling exponent $y = 1/(-\lambda+\alpha+2)$ [Eq. (2.16)]. By matching the initial and late time relations one has at the cross-over $\mathcal{R}^{\gamma}\theta_c^{\beta} \approx \kappa^{-y}\theta_c^{y}$, i.e. $\theta_c \approx \mathcal{R}^{-\gamma/\omega}\kappa^{-y/\omega}$, where $\omega = \beta - y$. Using this value for the cross-over coverage one has

$$\bar{s} \sim \left(\frac{\kappa}{\theta_c}\right)^{-y} \Theta^{y}\Psi(\Theta), \tag{A.7}$$

where $\Theta = \theta/\theta_c$, and the scaling function $\Psi(\Theta)$ behaves as

$$\Psi(\Theta) \sim \begin{cases} \Theta^{\omega}, & \Theta \ll 1; \\ \psi_0 & \Theta \gg 1, \end{cases} \tag{A.8}$$

where ψ_0 is a constant.

Appendix B

Growth rate in radial geometry

In radial geometry the Helmholtz equation (3.2) and the boundary conditions (3.3)–(3.5) keep their forms. The solution at the terrace bounded by the perfect circular steps at R and $R+L$ becomes [57] $u_0(r) = A_0 I_0(r/x_s) + B_0 K_0(r/x_s)$, where $R \leq r \leq R+L$ is the distance from the origin, and $I_0(x)$ and $K_0(x)$ are the modified Bessel functions of order zero. The coefficients A_0 and B_0 determined by the boundary conditions are $A_0 = -K_0'(R+L)\left[\Gamma/R - \tau\Delta\Phi\right]/C_0; B_0 = I_0'(R+L)\left[\Gamma/R - \tau\Delta\Phi\right]/C_0; C_0 = K_0(R)I_0'(R+L) - K_0'(R+L)I_0(R)$, where the prime indicates the derivative and all arguments of the modified Bessel functions have been scaled with x_s.

A linear stability analysis in radial geometry is performed by making a time-dependent perturbation at both steps which bound the terrace. The perturbation is given by:

$$\tilde{r}_j(\theta) = R_j + \epsilon \exp(\mathrm{i}n\theta + \omega t), \tag{B.1}$$

where R_j is the radius of the jth terrace, ϵ is a small parameter, $|n| \geq 1$ denotes the number of fluctuations at the step, θ is an angle, and ω is the growth rate. Consider the terrace between the steps at R and $R+L$. The solution to first order in ϵ is:

$$u(r,\theta) = u_0(r) + \epsilon\left[A_n I_n(r/x_s) + B_n K_n(r/x_s)\right]\exp(\mathrm{i}n\theta + \omega t), \tag{B.2}$$

where $I_n(x)$ and $K_n(x)$ are the modified Bessel functions of order n. The coefficients A_n and B_n are determined by the boundary conditions.

Consider for example the case where $k_+ \to \infty$ and $k_- \to 0$, corresponding to instantaneous attachment from the lower terrace and an infinite ES barrier

in the upper terrace. In this limit the boundary conditions for $u(r)$ simplify:

$$\begin{aligned} u(r)\,|_+ &= \Gamma\kappa - \tau\Delta\Phi; \\ \nabla u(r)\cdot\mathbf{n}\,|_- &= 0; \\ V = V_+ + V_- = D\nabla u(r)\cdot\mathbf{n}\,|_+ &= V_0 + \omega\epsilon\exp[\mathrm{i}n\theta + \omega t], \end{aligned}$$

where the curvature is given by [100] $\kappa(r) = \frac{1}{r} - \frac{\epsilon}{r^2}(1-n^2)\exp[\mathrm{i}n\theta + \omega t]$, when expanded to the first order in ϵ. The boundary conditions lead to the matrix equation for the coefficients:

$$\begin{pmatrix} I_n'(R+L) & K_n'(R+L) & x_{13} \\ I_n(R) & K_n(R) & x_{23} \\ I_n'(R) & K_n'(R) & x_{33} \end{pmatrix} \begin{pmatrix} A_n \\ B_n \\ \epsilon \end{pmatrix} = 0,$$

where the last column is given by

$$\begin{aligned} x_{13} &= B_0\left[K_0''(R+L)I_0'(R+L) - K_0'(R+L)I_0''(R+L)\right]/[x_s I_0'(R+L)]; \\ x_{23} &= B_0\left[K_0'(R)I_0'(R+L) - K_0'(R+L)I_0'(R)\right]/[x_s I_0'(R+L)]; \\ x_{33} &= x_{13} - \omega\sqrt{\Omega^2\tau/D}, \end{aligned}$$

where all arguments have been scaled with x_s. The matrix equation has non-trivial solutions [i.e. solutions other than $(A_n, B_n, \epsilon) = (0,0,0)$] if the determinant of the matrix is zero. After some algebra one ends up with the expression for the growth rate:

$$\frac{\omega(n)}{\Omega\Delta\Phi} = \frac{b_n^1 + b_n^2 + b_n^3}{a_n} + c_n\frac{\xi_s x_s^2}{R^2}(1-n^2), \tag{B.3}$$

where $\xi_s = \Gamma/(x_s\tau\Delta\Phi)$, and the coefficients are given by

$$\begin{aligned} a_n &= [\widehat{I}_n' K_n - I_n\widehat{K}_n'][\widehat{I}_1 K_0 + I_0\widehat{K}_1]; \\ b_n^1 &= [\widehat{I}_n' K_n - I_n\widehat{K}_n'][I_1'\widehat{K}_1 - \widehat{I}_1 K_n']; \\ b_n^2 &= [I_n'\widehat{K}_n' - \widehat{I}_n' K_n'][I_1\widehat{K}_1 - \widehat{I}_1 K_n]; \\ b_n^3 &= [I_n' K_n - I_n' K_n][\widehat{I}_1'\widehat{K}_1 - \widehat{I}_1\widehat{K}_n']; \\ c_n &= [\widehat{I}_n' K_n - I_n\widehat{K}_n'][\widehat{I}_n' K_n - I_n\widehat{K}_n'], \end{aligned}$$

where $I_n = I_n(R)$, $\widehat{I}_n = I_n(R+L)$, and similarly for K_n. If $\omega > 0$ the step edge is linearly unstable against meandering, otherwise it is stable. Using asymptotic forms of the modified Bessel functions for large n Eq. (B.3) reduces back to the BZ expression in the limit $n, R \to \infty$, where $q = n/R$ remains constant.

Bibliography

[1] M. Rusanen, J. Asikainen, and I.T. Koponen, unpublished.

[2] H. Brune, *Surf. Sci. Rep.* **31**, 121 (1998).

[3] A.-L. Barábasi and H.E. Stanley, *Fractal Concepts In Surface Growth* (Cambridge University Press, Cambridge, 1995).

[4] M.A. Herman and H. Sitter, *Molecular Beam Epitaxy* (Springer, Heidelberg, 1996).

[5] J. Krug, *Adv. Phys* **46**, 139 (1997).

[6] J. Tersoff, A.W. Denier van der Gon, and R.M. Tromp, *Phys. Rev. Lett.* **72**, 266 (1994).

[7] J. Rottler and P. Maass, *Phys. Rev. Lett.* **83**, 3490 (1999); J. Krug, P. Politi and T. Michely, *Phys. Rev. B* **61**, 14037 (2000).

[8] S. Esch, M. Breeman, M. Morgenstern, T. Michely, and G. Comsa, *Surf. Sci.* **365**, 187 (1996).

[9] M.V. Ramana Murty, *Surf. Sci.* **500**, 523 (2002).

[10] E. Chason and B.K. Kellermann, *Nucl. Inst. Meth. Phys. Res. B*, **127-128**, 225 (1997); W. Ensinger, *ibid.* **127-128**, 796 (1997).

[11] R. Kunkel, B. Poelsema, L.K. Verheij, and G. Comsa, *Phys. Rev. Lett.* **65**, 733 (1990).

[12] P. Šmilauer, M.R. Wilby, and D.D. Vvedensky, *Phys. Rev. B* **47**, 4119 (1993).

[13] P.G.J. van Dongen and M.H. Ernst, *Phys. Rev. Lett.* **54**, 1396 (1985).

[14] P. Jensen, A.-L. Barábasi, H. Larralde, S. Havlin, and H.E. Stanley, *Phys. Rev. B* **50**, 15316 (1994).

[15] C. Ratsch, A. Zangwill, P. Šmilauer, and D.D. Vvedensky, *Phys. Rev. Lett.* **72**, 3194 (1994).

[16] M.C. Bartelt and J.W. Evans, *Phys. Rev. B* **46**, 12675 (1992).

[17] G.S. Bales and D.C. Chrzan, *Phys. Rev. B* **50**, 6057 (1994).

[18] M. Rost, P. Šmilauer, and J. Krug, *Surf. Sci.* **369**, 393 (1996).

[19] G.S. Bales and A. Zangwill, *Phys. Rev. B.* **41**, 5500 (1990); *Phys. Rev. B* **48**, 2024 (1993).

[20] O. Pierre-Louis, M.R. D'Orsogna, and T.L. Einstein, *Phys. Rev. Lett.* **82**, 3661 (1999).

[21] Y.W. Mo, J. Kleiner, M.B. Webb, and M.G. Lagally, *Phys. Rev. Lett.* **66**, 1998 (1991).

[22] J.A. Venables, G.D.T. Spiller, and M. Hanbücken, *Rep. Prog. Phys.* **47**, 399 (1984).

[23] J. Villain, A. Pimpinelli, L. Tang, and D.E. Wolf, *J. Phys. I (France)* **2**, 2107 (1992).

[24] A. Pimpinelli and J. Villain, *Physics of Crystal Growth* (Cambridge University Press, Cambridge, 1998).

[25] P. Kratzer and M. Scheffler, *Phys. Rev. Lett.* **88**, 036102 (2002).

[26] K.A. Fichthorn and M. Scheffler, *Phys. Rev. Lett.* **84**, 5371 (2000).

[27] P. Politi, *J. Phys. I (France)* **7**, 797 (1997).

[28] P. Politi, G. Grenet, A. Marty, A. Ponchet, and J. Villain, *Phys. Rep.* **324**, 271 (2000).

[29] T. Vicsek and F. Family, *Phys. Rev. Lett.* **52**, 1669 (1984).

[30] D. Stauffer and A. Aharony, *Introduction to Percolation Theory* (Taylor and Francis, London, 1992).

[31] I. Koponen, M. Rusanen, and J. Heinonen, *Phys. Rev. E* **58**, 4037 (1998).

[32] M. von Smoluchowski, *Phys. Z.* **17**, 585 (1916).

[33] J. Feder, T. Jøssang, and E. Rosenqvist, *Phys. Rev. Lett.* **53**, 1403 (1984).

[34] S. Ispolatov, P.L. Krapivsky, and S. Redner, *Eur. Phys. J. B* **2**, 267 (1998).

[35] J. Silk and S.D. White, *Astrophys. J.* **223**, L59 (1978).

[36] S. Chandrasekhar, *Rev. Mod. Phys.* **15**, 1 (1943).

[37] P.G.J. van Dongen, *J. Stat. Phys.* **53**, 221 (1988); *ibid.* **54**, 221 (1989); *ibid.* **58**, 87 (1990).

[38] N. G. van Kampen, *Stochastic Processes in Physics and Chemistry*, 2nd ed. (North–Holland, Amsterdam, 1992).

[39] M.H. Ernst, in *Fractals in Physics*, edited by L. Pietronero and E. Tosatti (Elsevier, Amsterdam, 1986), p. 289.

[40] S. Ovesson, *Phys. Rev. Lett.* **88**, 116102 (2002).

[41] M.C. Bartelt and J.W. Evans, *Phys. Rev. B* **54**, R17359 (1996).

[42] P.A. Mulheran and J.A. Blackman, *Phys. Rev. B* **53**, 10261 (1996).

[43] J.G. Amar, M.N. Popescu and F. Family, *Phys. Rev. Lett.* **86**, 3092 (2001); *Surf. Sci.* **491**, 239 (2001); M.N. Popescu, J.G. Amar, and F. Family, *Phys. Rev. B* **64**, 205404 (2001).

[44] F. Family, P. Meakin, and J.M. Deutch, *Phys. Rev. Lett.* **57**, 727 (1986).

[45] C.M. Sorensen, H.X. Zhang, and T.W. Taylor, *Phys. Rev. Lett.* **59**, 363 (1987).

[46] P.G.J. van Dongen and M.H. Ernst, *J. Stat. Phys.* **37**, 301 (1984).

[47] P. Meakin and M.H. Ernst, *Phys. Rev. Lett.* **60**, 2503 (1988).

[48] M.H. Ernst and P.G.J. van Dongen, *Phys. Rev. A* **36**, 435 (1987).

[49] G.S. Bales and A. Zangwill, *Phys. Rev. B* **55**, R1973 (1997).

[50] J.A. Blackman and A. Marshall, *J. Phys. A: Math. Gen.* **27**, 725 (1994).

[51] P.L. Krapivsky, J.F.F. Mendes, and S. Redner, *Eur. Phys. J. B* **4**, 401 (1998).

[52] G. Ehrlich and F.G. Hudda, *J. Chem. Phys.* **44**, 1039 (1966).

[53] R. L. Schwoebel and E. J. Shipsey, *J. Appl. Phys.* **37**, 3682 (1966).

[54] J. Villain, *J. Phys. I (France)* **1**, 19 (1991).

[55] R.L. Schwoebel, *J. Appl. Phys.* **40**, 614 (1969).

[56] J. Krug, *J. Stat. Phys.* **87**, 505 (1997).

[57] W. K. Burton, N. Cabrera, and F. C. Frank, *Phil. Trans. R. Soc. London, Ser. A* **243**, 299 (1951).

[58] W.W. Mullins and R.F. Sekerka, *J. Appl. Phys.* **35**, 444 (1964).

[59] R. Ghez and S.S. Iyer, *IBM J. Res. Develop.* **32**, 804 (1988).

[60] L.D. Landau and E.M. Lifshitz, *Statistical Physics*, 3rd ed. (Butterworth-Heineman, Oxford, 1980).

[61] J. Kallunki and J. Krug, *Phys. Rev. B* **62**, 6229 (2000); F. Gillet, O. Pierre-Louis and C. Misbah, *Eur. Phys. J. B* **18**, 519 (2000).

[62] L. Schwenger, R.L. Folkerts, and H.-J. Ernst, *Phys. Rev. B* **55**, R7406 (1997).

[63] T. Maroutian, L. Douillard, and H.-J. Ernst, *Phys. Rev. Lett.* **83**, 4353 (1999); *Phys. Rev. B* **64**, 165401 (2001).

[64] T. Salditt and H. Spohn, *Phys. Rev. E* **47**, 3524 (1993).

[65] M.V. Ramana Murty and B.H. Cooper, *Phys. Rev. Lett.* **83**, 352 (1999).

[66] J. Kallunki, J. Krug, and M. Kotrla, *Phys. Rev. B* **65**, 205411 (2002).

[67] J. Merikoski, I. Vattulainen, J. Heinonen, and T. Ala-Nissila, *Surf. Sci.* **387**, 167 (1997).

[68] A.M. Cadilhe, C.R. Stoldt, C.J. Jenks, P.A. Thiel, and J.W. Evans, *Phys. Rev. B* **61**, 4910 (2000).

[69] F.B. de Mongeot, G. Costantini, C. Boragno, and U. Valbusa, *Europhys. Lett.* **58**, 537 (2002).

[70] J. Kallunki and J. Krug, e-print cond-mat/0208512 (2002).

[71] P. Politi and J. Krug, *Surf. Sci.* **446**, 89 (2000).

[72] I. Elkinani and J. Villain, *J. Phys. I (France)* **4**, 949 (1994).

[73] P. Politi and J. Villain, *Phys. Rev. B* **54**, 5114 (1996).

[74] O. Pierre-Louis, C. Misbah, Y. Saito, J. Krug, and P. Politi, *Phys. Rev. Lett.* **80**, 4221 (1998).

[75] A. B. Bortz, M. H. Kalos, and J. L. Lebowitz, *J. Comput. Phys.* **17**, 10 (1975).

[76] K. Kang and S. Redner, *Phys. Rev. A* **30**, 2833 (1984); K. Kang, S. Redner, P. Meakin, and F. Leyvraz, *ibid.* **33**, 1171 (1986).

[77] N.W. Ashcroft and N.D. Mermin, *Solid State Physics* (Holt, Rinehart, and Winston, New York, 1976).

[78] D.P. Landau and K. Binder, *A Guide to Monte Carlo Simulations in Statistical Physics* (Cambridge University Press, Cambridge, 2000).

[79] J.D. Muños, M.A. Novotny, and S.J. Mitchell, e-print cond-mat/0211164 (2002).

[80] M. Kotrla, *Comput. Phys. Comm.* **97**, 82 (1995).

[81] J. L. Blue, I. Beichl, and F. Sullivan, *Phys. Rev. E* **51**, 867 (1995).

[82] R. Botet, R. Jullien, and M. Kolb, *J. Phys. A* **17**, L75 (1984); *Phys. Rev. A* **30**, 2150 (1984).

[83] E. Adam, L. Billard, and F. Lancon, *Phys. Rev. E* **59**, 1212 (1999).

[84] A.F. Voter, *Phys. Rev. B* **34**, 6819 (1986); S.V. Khare, N.C. Bartelt, and T.L. Einstein, *Phys. Rev. Lett.* **75**, 2148 (1995); W.W. Pai, A.K. Swan, Z. Zhang, and J.F. Wendelken, *Phys. Rev. Lett.* **79**, 3210 (1997); L. Bitar, P.A. Serena, P. García-Mochales, N. García, and V.T. Binh, *Surf. Sci.* **339**, 221 (1995).

[85] J. Heinonen, I. Koponen, J. Merikoski, and T. Ala-Nissila, *Phys. Rev. Lett.* **82**, 2733 (1999).

[86] J. Sillanpää and I. Koponen, *Nucl. Inst. Meth. B* **142**, 67 (1998).

[87] L. Kuipers and R.E. Palmer, *Phys. Rev. B* **53**, R7646 (1996).

[88] P.G.J. van Dongen, *Phys. Rev. Lett.* **63**, 1281 (1989).

[89] C.-H. Choi, R. Ai, and S.A. Barnett, *Phys. Rev. Lett.* **67**, 2826 (1991); B.K. Kellerman, E. Chason, J.A. Floro, S.T. Picraux, and J.M. White, *Appl. Phys. Lett.* **67**, 1703 (1995); S. Esch, M. Bott, T. Michely, and G. Comsa, *ibid.* **67**, 3209 (1995); M. Kalf, M. Breeman, M. Morgenstern, T. Michely, and G. Comsa, *ibid.* **70**, 182 (1997).

[90] M. Rusanen, I. Koponen, J. Heinonen, and J. Sillanpää, *Nucl. Inst. Meth. Phys. Res. Sec. B* **148**, 116 (1999).

[91] N. Israeli and D. Kandel, *Phys. Rev. Lett.* **80**, 3300 (1998); *Phys. Rev. B* **60**, 5946 (1999).

[92] P. Finnie and Y. Homma, *Phys. Rev. Lett.* **85**, 3237 (2000); Y. Homma and P. Finnie and M. Uwaha, *Surf. Sci.* **492**, 125 (2001).

[93] M. Rusanen, I.T. Koponen, and T. Ala-Nissila, *Surf. Sci.* **507-510**, 305 (2002).

[94] A. Pimpinelli, I. Elkinani, A. Karma, C. Misbah, and J. Villain, *J. Phys. C: Cond. Matt.* **6**, 2661 (1994).

[95] J. Krug and M. Schimschak, *J. Phys. I (France)* **5**, 1065 (1995).

[96] M. Rusanen, I.T. Koponen, J. Heinonen, and T. Ala-Nissila, *Phys. Rev. Lett.* **86**, 5317 (2001).

[97] M. Rusanen, I.T. Koponen, T. Ala-Nissila, C. Ghosh, and T.S. Rahman, *Phys. Rev. B* **65**, 041404 (2002).

[98] M. Rusanen, I.T. Koponen, and J. Kallunki, submitted to Surface Science (2002).

[99] A. Karma and M. Plapp, *Phys. Rev. Lett.* **81**, 4444 (1998).

[100] S.V. Khare and T.L. Einstein, *Phys. Rev. B* **54**, 11752 (1996).